Nanoscale Magnetometry with Single Fluorescent Nanodiamonds Manipulated in an Anti-Brownian Electrokinetic Trap

THÈSE N^O 6972 (2016)

PRÉSENTÉE LE 11 MARS 2016
À LA FACULTÉ DES SCIENCES ET TECHNIQUES DE L'INGÉNIEUR
LABORATOIRE DE BIOLOGIE À L'ÉCHELLE NANOMÉTRIQUE
PROGRAMME DOCTORAL EN PHOTONIQUE

ÉCOLE POLYTECHNIQUE FÉDÉRALE DE LAUSANNE

POUR L'OBTENTION DU GRADE DE DOCTEUR ÈS SCIENCES

PAR

Metin KAYCI

acceptée sur proposition du jury:

Prof. H. Altug Yanik, présidente du jury
Prof. A. Radenovic, directrice de thèse
Prof. M. Krishnan , rapporteuse
Prof. R. Goldsmith, rapporteur
Prof. C. Degen , rapporteur

EPFL

ÉCOLE POLYTECHNIQUE
FÉDÉRALE DE LAUSANNE

Suisse
2016

Abstract

Studies on single-molecule spectroscopy and nanoscale detection have been remarkably driven by an interest to reveal quantum and conformational states of single particles, the intra-molecular dynamics and their response to physical observables hidden by ensemble level measurements. A straightforward practice used in enhancing the signal from single particles is either to immobilize them on an engineered substrate or to embed them in a solid matrix. Given that the biophysical properties of the host environment introduce new perturbations and the particles will not behave as in their native environment, such approaches are inefficient to reflect the real dynamics. Therefore, recent advances in the field of single-molecule have led to a renewed interest in novel trapping methods, increased efforts into the development of promising tools for extended investigation, and the manipulation of solution-phase bio-molecules in real time. Despite the variety of successful passive trapping techniques, precise manipulation through non-perturbative forces is a big challenge for nano-sized particles. Such techniques either exert high power to the sample or compel special operating conditions disturbing the native environment. Therefore, an active trapping scheme guiding non-perturbative forces can break the trade-off between the particle size and the excreted power.

This dissertation presents the development of an active trapping set-up using non-perturbative electrokinetic feedback and demonstrates its performance on nano-sized single particles for aims in biophysics. The essential theme is the engineering aspect of the technique, including the feedback configurations for various fluidic devices, the corresponding particle tracking schemes and the integration of the trapping platform to an integrated circuit pattern for advanced manipulation aims. The second theme is on specialized single fluorescence nanodiamonds (FNDs) as scanning magnetometer in fluidics. The implemented active trapping tool is employed for the manipulation of a rotationally free single FND to detect the localized magnetic field through an optically detected magnetic resonance (ODMR) spectrum. While the laser beam used in particle tracking can serve in optical excitation, an external radio frequency (RF) source is not sufficient to achieve microwave manipulation. Therefore, an RF antenna is designed to transmit the microwave signal to the proximity of the trapping chamber for electron spin resonance (ESR) spectroscopy. A nanostage positioning controller introduces scanning ability to the sample plane, in relative position of the trapped particle, in order to map the distribution of the detected fields over a fluidic volume. As FNDs are also sensitive to many other physical quantities, nanoscale single particle trapping and

diamond photonics linkages are realized in this work, which provide an outstanding alternative for detection and imaging in complex fluidic environments that are closed to AFM-like physically supported probes.

Résumé

Les études de spectroscopie à une seule molécule et la détection à l'échelle nano ont été remarquablement dominées par un intérêt à révéler les états quantique ou conformationnels de particules individuelles, la dynamique intramoléculaire et la réponse à certaines observables physiques cachées par des mesures d'ensemble. Les particules individuelles, isolées, immobilisés sur un substrat ou encastrées dans une matrice solide est une pratique simple utilisée pour améliorer ce genre de mesures. Étant donné que les propriétés biophysiques de l'environnement hôte introduisent de nouvelles perturbations et les particules ne se comporteront pas comme dans leur environnement natif, ces approches sont inefficaces pour refléter la dynamique réelle. Par conséquent, les progrès récents dans le domaine de la molécule unique ont conduit à un regain d'intérêt dans de nouvelles méthodes de piégeage et de grands efforts ont été consacrés à l'élaboration d'outils prometteurs pour l'enquête approfondie et la manipulation des bio-molécules en phase solution et en temps réel. Bien qu'une grande variété de techniques de piégeages passifs ont été démontrés, la manipulation précise grâce à des forces non-perturbatrices est un grand défi pour les particules de taille nanométrique. Ces techniques exercent soit une puissance élevée à l'échantillon ou impliquent des conditions particulières perturbant l'environnement natif. Au lieu de cela, un système de piégeage actif guidant des forces non perturbatrices peut briser le compromis entre la taille des particules et la puissance excrétée.

Cette thèse présente le développement d'une installation de piégeage actif en utilisant des feedback électro cinétique non perturbateurs et démontre sa performance sur les particules individuelles de taille nanométrique pour objectifs biophysique. Le thème essentiel est l'aspect technique, y compris les configurations de feedback pour divers dispositifs fluidiques, les systèmes de suivi des particules correspondantes et l'intégration de la plate-forme de piégeage à un modèle de circuit intégré pour des installations de manipulation. Le deuxième thème est les nano diamants fluorescent (FNDS) en tant que magnétomètre en fluidique. L'outil de piégeage actif est mis en œuvre dans la manipulation d'un seul FND libre en rotation pour détecter le champ magnétique local par résonance magnétique optiquement détecté (ODMR). Alors que le faisceau laser utilisé dans le suivi des particules peut servir à une excitation optique, une fréquence radio externe (RF) n'est pas suffisante pour atteindre la manipulation de micro-ondes. Par conséquent, une antenne RF est conçue pour transmettre le signal hyperfréquence à la proximité de la chambre de piégeage pour une résonance de spin électronique (ESR) par spectroscopie. Un dispositif de positionnement nano introduit la capacité de

balayage de l'échantillon, et donc également la position relative de la particule piégée, pour cartographier la distribution des champs détectés sur un volume de fluide. Comme FNDS sont également sensibles à beaucoup d'autres grandeurs physiques, le piégeage des particules nanométrique lié à la photonique de diamant réalisée dans ce travail fournit une excellente alternative pour la détection et l'imagerie dans des environnements fluidiques complexes qui sont fermés aux sondes purement physique comme l'AFM.

Mots-clés: Microfluidique, anti-Brownien électrocinétique trappe (ABEL), résonance de spin électronique (RSE), nanodiamants fluorescents, vacance d'azote, magnétométrie à l'échelle nanométrique.

Acknowledgements

First of all, I would like to thank my thesis director Prof. Aleksandra Radenovic who gave me the opportunity to pursue a PhD in her lab and provided a comfortable research environment. She always encouraged me to implement creative ideas into my work. It would not have been possible to complete this work without her guidance, and support.

I would like to thank the jury members of my thesis committee for taking the time to read and giving constructive feedbacks.

I would like to thank all my colleagues for the nice atmosphere in the lab and lots of helpful advices.

Finally, I would like to present my special thanks to my family for their love, encouragement and continuous support. I owe them a lot.

Thesis Outline

Chapter 1 presents a detailed description of the set-up used for single particle trapping in microfluidics. The Brownian motion and the counteracting forces generated in microfluidics for position control are briefly summarized. Given that nanoscale particles are diffusing very fast and camera-based solutions are not efficient for monitoring, a laser-guided scheme is used for positon detection. The scanning excitation, the confocal detection and the digital filter employed in transversal position estimation are the main issues focused in this chapter.

Chapter 2 is content reproduced verbatim from a submitted book chapter on single fluorescence nanodiamonds (FNDs), which reviews studies on nitrogen vacancy defects embedded in FNDs and their applications in mapping and sensing physical quantities. The working principles of the applications are illustrated through the outstanding spin and optical properties that the defect introduces. The manipulation techniques proposed in the literature are compared to the one employing electrokinetic forces.

Chapter 3 is content reproduced verbatim from a published work on three-dimensional single particle manipulation. It presents the hybrid approach used in positon detection and the novel microfluidic configuration used for three-dimensional feedback. It is shown that the off-focus fluorescence profile of a nanoscale particle can be image-processed to extract its axial position. Then, the corresponding feedback can be applied through a cascaded thin PDMS layer coupling the electrokinetic forces into the axial dimension.

Chapter 4 is content reproduced verbatim from a published work on single FNDs in ABEL trap. It is shown that ABEL trap technique is compatible to electron spin resonance (ESR) experiments carried on single FNDs. The design of a radio frequency antenna for microwave excitation and its integration to the trapping platform is presented. With the link provided in this work, it is demonstrated that sensing and imaging capabilities of single FNDs can be exploited in environments where other manipulation techniques are not functional. The approach is validated through magnetic field sensing in closed microfluidics.

Chapter 5 summarizes the complete work done in this PhD thesis and puts it into perspective by describing possible future directions.

Contents

1. Introduction

Positon control and manipulation of a single particle in solution phase plays a major role for studying fundamental problems in various fields of research. For instance, through the changes in the fluorescence signal, one can investigate the inner dynamics of a particle that is not resolvable in ensemble level averaging. Given that the conformational states of a protein determine its functionality and contribute to the fluorescence profile, single particle manipulation provides a remarkable tool for cell biology and pharmacological research. Furthermore, by position control of a sensitive particle in a local volume, one can resolve the physical quantities in the environment and map the distributions through the particle response. In other words, with the scanning ability a functional nanoscale particle can act as biophysical sensor resolving environmental characteristics.

With these motivations, there are a number of techniques exploiting different schemes for the manipulation of single particles, see **section 1.2.** Unfortunately, such techniques fail to provide precise measurements on nanoscale particles either due to the restrictions on particle properties and operating conditions or due to the perturbations they introduce to the environment. Therefore, the first objective of this PhD work aims to realize an active trapping platform cancelling the Brownian motion through the electrokinetic forces in microfluidics. Precise single particle tracking at high temporal resolution and following active control are the main approaches used for the manipulation, see **section 1.3.** Unlike passive approaches, the platform applies electrokinetic forces in a smart manner, so that the manipulation is not perturbative and operational on all optically traceable nanoparticles in solution.

Once the position control has been achieved, we employed the platform in the manipulation of nitrogen vacancy (NV) centres in single fluorescent nanodiamonds (FNDs) for scanning magnetometry application. Non-perturbative manipulation of nanoscale particles without any physical support and single particle level position control in closed fluidics are the key advantages over the other approaches used in single FNDs manipulation, see **section 2.6.**

1.1 Brownian Motion

Although the discovery of Brownian motion is attributed to Robert Brown for his work on pollen grains suspended in water [1], he was not the first to observe the phenomenon. Jan Ingenhousz reported the fluctuations in motion of suspended coal dust particles in 1765. The stochastic

movements of the molecules in the medium introduce non-directed forces on the suspended particle. Therefore, the Brownian motion of the particle is generally measured through the mean-square displacement over time. In 1905, Einstein published a work that predicted the relationship between the mean-square displacement and size of the particle [2]. 1926 when Jean Perrin was awarded the Nobel Prize in Physics for his experimental work on the Brownian motion [3]. Since then there have been many works confirming Einstein's hypothesis. Recently, to reveal the chaotic dynamics of the medium at microscopic scale, the position measurement of a suspended colloidal particle has been performed with high precision [4]. Here, the mean square displacement of such a particle will be analyzed through a discrete system perspective.
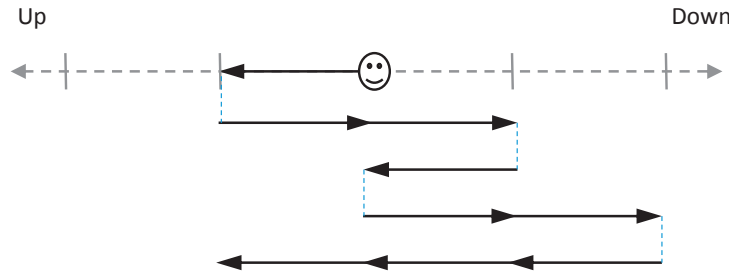
Figure 1.1: A random walker following DUUDUUDDD pattern has the parameters n=1, m=9 leading one-step up on the ladder.

A particle subjected to one dimensional Brownian motion follows a trajectory that one can expect from a random walker on a ladder, either choosing up (U) or down (D) steps with equal probabilities, i.e. one possible trajectory is shown in **Figure 1.1**. Then, the probability of n-step displacement after m-steps of walk is

$$P(n,m) = m! \, 2^{-m} / (\tfrac{m-n}{2})! \, (\tfrac{m+n}{2})! \tag{1.1.1}$$

Applying Stirling`s approximation [5] for big factorials, $z! = \sqrt{2\pi z}(\tfrac{z}{e})^z$,

$$P(n,m) = \frac{\sqrt{2/\pi m}}{(1+\frac{n}{m})^{(m+n)/2}(1-\frac{n}{m})^{(m-n)/2}\sqrt{1-n^2/m^2}} \tag{1.1.2}$$

Then, using Taylor series to the second order, for z≪ 1, $\ln(1+z) \approx z - z^2/2$

$$\ln P(n,m) - \ln\sqrt{\frac{2}{\pi m}} = \frac{-n^2}{2m}$$

$$P(n,m) = \sqrt{2/\pi m}\, e^{-n^2/2m} \tag{1.1.3}$$

Provided that each step leads to a distance change of l in a time bin of τ, the equation can be expressed in a continuous form probability density,

$$x = nl, t = m\tau$$

$$P(x,t) = \frac{e^{-x^2/4Dt}}{\sqrt{4\pi Dt}} \tag{1.1.4}$$

where $D = l^2/2\tau$ is the diffusion constant of the walker. Given that the random walks along orthogonal dimensions are uncorrelated, the mean-square displacement of 1D and 3D walk are $\langle x^2 \rangle = 2Dt$ and $\langle r^2 \rangle = 6Dt$, respectively. As Einstein-Smoluchowski's equation relates, the diffusion constant to the size of the suspended particle r and the viscosity of medium η, one can predict the mean-square displacement of a particle within a given time period.

$$D = \frac{k_b T}{6\pi r \eta} \tag{1.1.5}$$

1.2 Manipulation Techniques for Aqueous Dispersions

Several manipulation techniques for single FNDs trapping and spatial scanning are compared in **section 2.6.** In this section, the working principle of the manipulation techniques that are used for general tasks will be provided.

Optical tweezers are the most popular method for micro and nano-manipulation exploiting optical forces generated through a tightly focused laser beam. The forces arise from the momentum transfer associated to the refraction, scattering, absorption, and reflection of the laser beam. When the size of the target particle is much larger than the wavelength of the beam, *Mie regime*, the forces can be estimated through ray optics [6]. Assuming that the refraction index of the particle is greater than the environment, the Gaussian beam profile results in a restoring force pushing the particle into the beam center in the transverse plane. While for the transverse plane the overall scattering force is negligible, it shifts the trapped particle slightly beyond the focal point in axial dimension (**Figure 1.2**). When the size is much smaller, *Rayleigh regime*, the forces can be estimated by treating the particle as a point dipole that is induced by the electric field. In this case, the gradient force is proportional to the gradient in the beam intensity. By using objective lenses with high numerical aperture, one can generate a steep gradient and trap particles down to tens of nanometers in size [7]. When the dimension of the trapped particle is comparable to the beam wavelength, both approaches are not valid. Instead, more complex electromagnetic theories are

used for the estimation of the optical forces [8]. Despite the functionality of optical tweezers for a wide range of particle sizes, they do have some drawbacks. For instance, the high optical power required for a stable trapping can result in photo-damage or local heating in bio-samples [9]. Furthermore, as the generated optical forces are passive, any dielectric particle can be trapped. Therefore, manipulation at the single particle level requires extremely low concentrations.
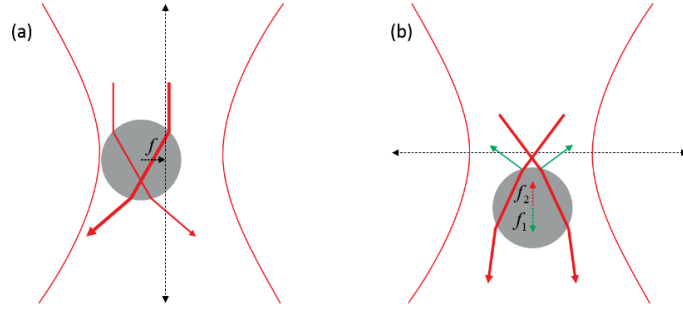

Figure 1.2: Schematic of optical tweezers illustrating the principle of trapping through ray optics. **a)** As the intensity of the refracting beam is larger in the center, the imparted momentum moves the particle towards the center in the transverse plane. **b)** The particle moves slightly above the focal point in the axial dimension due to the reflection (f_1) and the refraction (f_2) components.

Even though optical tweezers are not practical due to the excreted power and size trade-off, electrostatic trapping provides another option [10]. In this technique the trapping resolution is limited by the charge state of the target particle rather than its size. Although this configuration is not feasible for three-dimensional active positioning and the trapping performance depends on buffer characteristics, it provides an outstanding option for nanoscale particle sorting into high density arrays and single particle level analysis for a long period of time.

Standing waves provide yet another possibility for micro-manipulation. In this technique, particles are trapped in low pressure nodes that are generated by interdigital transduces. Recently, two-dimensional manipulation of single particles has been demonstrated [11]. The radiation force of plane waves depends on the target size; hence, filtering and sorting applications [12] are also possible. In contrast to optical tweezer, acoustic tweezers that employ standing waves are not sourcing local heating or photo-damage, so long term manipulation is possible. Although this approach is biocompatible and non-invasive, it is not viable for nanoscale manipulation. Further, excluding the complex versions, precise manipulation on an arbitrary path is not practical.

Hydrodynamic actuation is a powerful approach for the manipulation of arbitrary particles that do not possess any specific chemical or physical properties. Recently, manipulation of submicron single particles has been demonstrated through active hydrodynamic flow control in microfluidics [13]. The difficulty in precise flow control is the main drawback of the technique. Also, the chip valves used in the active feedback bring additional complexity to the fabrication process of the microfluidics.

Although not very popular, aqueous Paul trapping is another alternative for manipulation. Basically, the Brownian motion of the target particle is suppressed through DC and radio frequency voltages that introduce a focusing and defocusing potential well for the particle. Recently, nanoscale manipulation of single particles has been demonstrated in aqueous [14]. The complex fabrication process of the device and instability of three-dimensional positioning are the main drawbacks of the technique.
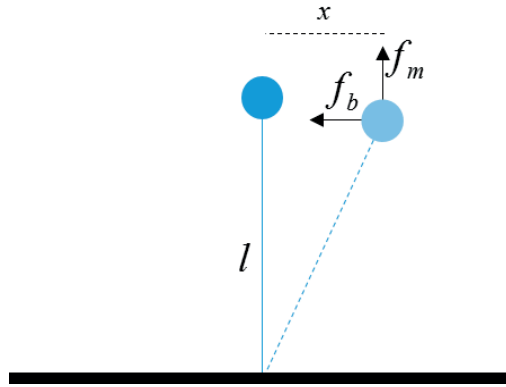
Figure 1.3: Inverted pendulum model for magnetic tweezers. The Brownian motion (horizontal) and the pulling force (vertical) are the two driving components for the trajectory of the magnetic bead. The restoring force and the mean energy for a spring are $f_b = kx$ and $E = k\langle x^2 \rangle/2$, respectively. Equipartition theorem for one-dimensional freedom, $E = k_b T$ and $f_b/f_m = x/l$, relation provides the pulling force as $f_b = lk_b T/\langle x^2 \rangle$.

Magnetic tweezers are simple yet versatile micromanipulation tools for excreting or measuring forces on single molecules. For instance, a functionalized DNA strand tethered to a magnetic bead will reflect the external magnetic field through the position displacement of the particle. A simple model, inverted pendulum, which describes the particle response, is shown in **Figure 1.3**. After the demonstration on single DNA molecules [15, 16], they have been widely used to investigate the dynamics of molecules such as recombinases [17], topoisomerases [18], and rotary motors [19]. Small permanent magnets [20] and sharp electromagnetic tips [21] are two common approaches used for the generation of a steep magnetic field gradient excreting high forces. Permanent magnet

configuration is very simple and useful for constant force experiments, but it lacks the ability of wide range positioning. Conversely, multiple electromagnet configuration [22] is a promising approach for three-dimensional manipulation as the generated force and its direction can be controlled through the current modulation and switching for active feedback. However, high driving current on electromagnets leads to hysteresis and heating that requires an active cooling system. Also, all magnetic tweezers' configurations are functional only if the target particle is paramagnetic or tethered to a paramagnetic particle.

Ultimately, all the techniques mentioned above either demand specific conditions for operation or are not functional for three-dimensional positioning at single particle level.

1.3 Electrokinetic Forces in Microfluidics

Electrophoresis and electroosmotic forces are the main components contributing to the electrokinetic mobility of a particle in aqueous medium when a potential is applied through the microfluidics (**Figure 1.4**).

For a charged particle, the balance between the Coulomb force and the drag force determines the electrophoresis velocity. For spherical objects, $f_{coulomb} = f_{drag}$, $6\pi\eta av = 4\pi\varepsilon\varepsilon_0 a\varsigma E$, where E is the electric field, ε_0 is the permittivity of free space, ς is the surface potential, η is the viscosity, ε is the dielectric constant of the fluid, v is the velocity, and a is the radius of the particle. Then, the electrophoresis mobility is $\mu_{ef} = 2\varepsilon\varepsilon_0\varsigma/3\eta$, which is known as Huckel's formula [23]. This phenomena has been extensively used for amino acid-protein separation [24, 25], drug analysis [26, 27], and DNA sequencing [28, 29].
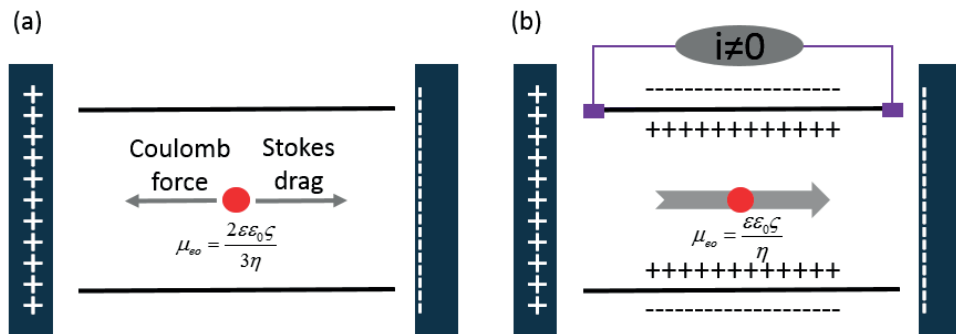

Figure 1.4: a) The forces contributing to the electrophoresis mobility. **b)** As a result of the applied potential, the mobile ions accumulated on negatively charged microfluidic surface generate a bulk flow.

When a potential is applied across the channel, a double layer of ions are formed on the charged microfluidic surface. Unlike the inner layer, the outer layer has mobile ions generating a bulk flow in the channel. This actuation introduces the electroosmotic mobility for the particle in the medium. Let σ be the charge density on the microfluidics surface. Then, the electric force per unit area on ions at Debye length, λ_d, is $f_e = \sigma E$ where $E = \varsigma/\lambda_d = \sigma/\varepsilon\varepsilon_0$. The viscosity force per unit area at l_d is given as $f = \eta\Delta v/\lambda_d$. In steady state, the equality of these two components provides the mobility $\mu_{eo} = \varepsilon\varepsilon_0\varsigma/\eta$, which is known as Smoluchowski's formula [30]. Recently, micro pumps for fluid cooling [31] and fluid mixing [32] have been proposed as potential applications employing electroosmotic control.

The overall mobility is generalized through Henry`s function [33] by scaling it with particle size and Debye length ratio, $\mu = f(\frac{a}{\lambda_d})\varepsilon\varepsilon_0\varsigma/\eta$. The main conclusion here is that for a given particle size and buffer viscosity, the mobility is constant. This allows a linear electrokinetic control over the position of a nanoscale particle. Instead of theoretical calculations, the mobility parameter can be extracted easily by monitoring the position response of such a particle on an applied electric field strength.

1.4 Anti-Brownian Electrokinetic (ABEL) Trap

The Anti-Brownian elelctrokinetic trap (ABEL trap) is a tool first invented by Adam Cohen and W.E. Moerner to manipulate single fluorescent molecules in solution phase [34-36]. As the name suggests, the objective is to cancel the Brownian motion by electrokinetic forces. The main challenge of such an active trapping tool is to track the Brownian motion of a nanoscale particle over a very short time period, where the particle is not able to escape. Since we are not interested in the imaging of a fluidic sample, but the tracking of a diffusing single particle and the mean square displacement of nanoscale particles is very high camera-based solutions are not practical. Instead, a scanning excitation laser beam with a very fast single photon counting module (SPCM) can provide the required tracking frequency. The working principle of a two-dimensional ABEL trap set-up is schematized in **Figure 1.5**. Basically, it consists of a scanning excitation, a confocal detection and a digital filter on a field programmable gate array (FPGA) device performing the position estimation and active feedback.
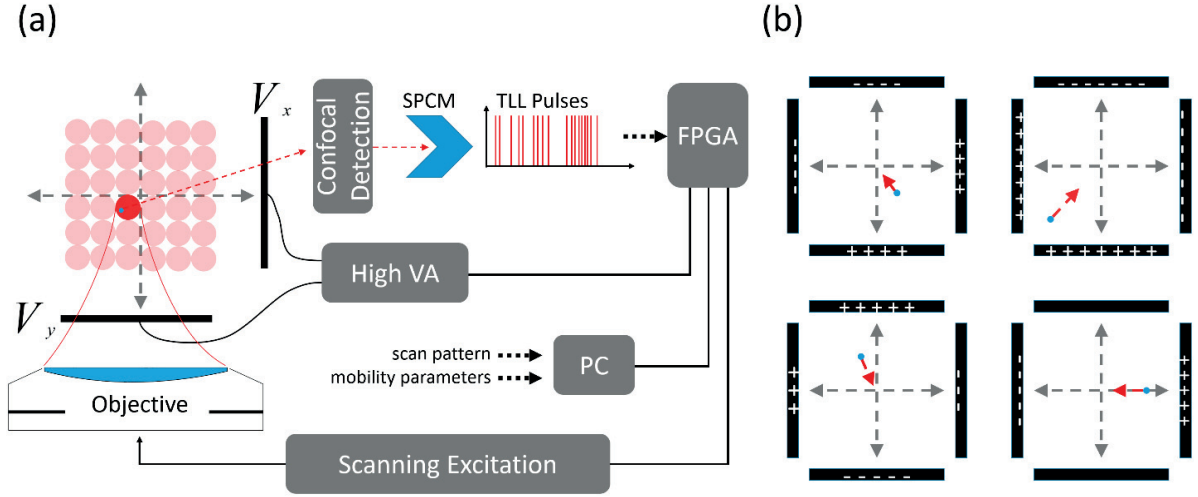
Figure 1.5: a) The schematic of ABEL Trap set-up. Scanning laser beam excitation and confocal detection SPCM perform the single particle tracking at 20 kHz. A digital filter on the FPGA device estimates the positon based on the photon count rate on the SPCM, laser beam scanning pattern, and particle mobility parameters. The position of the particle is controlled through physical voltages applied to the electrodes V_x, V_y. **b)** Active electrokinetic feedback concept. Depending on the Brownian motion induced displacement, the physical voltages applied to the electrodes generate an electric field vector that moves the particle back to the target point.

In the following subsections I will outline some of the unique designs I implemented for the realization of ABEL trap presented in this thesis.

1.4.1 Excitation Optics

The electro optic deflectors (EODs) are the key components in the excitation optics. Depending on the physical voltages applied to the high voltage amplifiers (HVAs), a linear refractive index gradient is formed through the crystals inside the EODs. This allows the FPGA device control to modulate the angle of the collimated beam at the output. The defined angles are mapped to positions in the sample plane through the relay lenses and microscope objective. The optic components are arranged so that a pencil-like beam (confocal length is high) with a small waist provides high resolution in scanning.
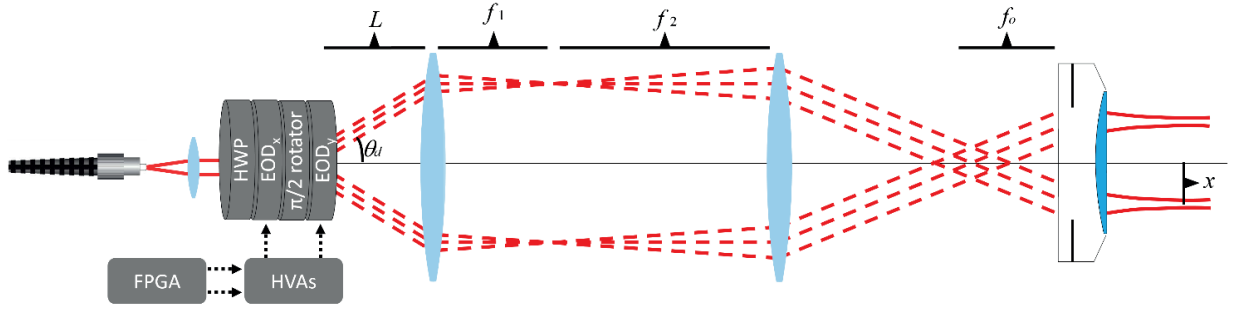
Figure 1.6: The optics performing excitation in scanning mode. The angles introduced with the EODs are mapped to linear positions in the sample plane through the relay lenses.

The beam waist formed through a microscope objective is $w_0 = \lambda/\pi\theta$, where θ defines the subtended angle [37] at the focus point and λ is the wavelength of the beam. A beam with a waist of w_1 entering the objective sets the angle as $\theta = w_1/f_0$, where f_0 states the objective focal length (see **Figure 1.7**). For a microscope objective with m magnification $f_0 = f_t/m$, where f_t defines the focal length of the tube lens. A beam waist of w_i passing through the relay lenses with focal length of f_1 and f_2 rescales as $w_1 = w_i f_2/f_1$. While a very small beam waist is possible with the given parameters the high confocal length [38] l_c requirement for a pencil-like beam is an important limiting factor $l_c = 2\pi w_0^2/\lambda$. Since EODs are operating at high physical voltages, HVAs are used to amplify the output voltages of the FPGA device. Then, the deflection angle is $\theta_d = k\gamma v$, where k is a constant γ is the gain of HVAs and v is the analog output of the FPGA device used for control. The deflection angle is converted to a position in the sample plane through the geometry provided by the intermediate optics, $x = Lf_0 \tan\theta_d/f_2$, where L is the distance to the first relay lens (**Figure 1.6**).

Figure 1.7: The confocal beam in the sample plane. The beam waist is a function of subtended angle.

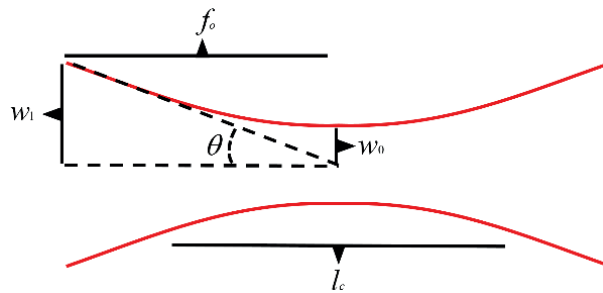With the specification given above, a laser beam with a waist of ≈0.8 µm and confocal length of ≈7 µm is used in this work to perform high resolution scanning over an area up to 20x20 µm² in the sample plane.

1.4.2 Detection Optics
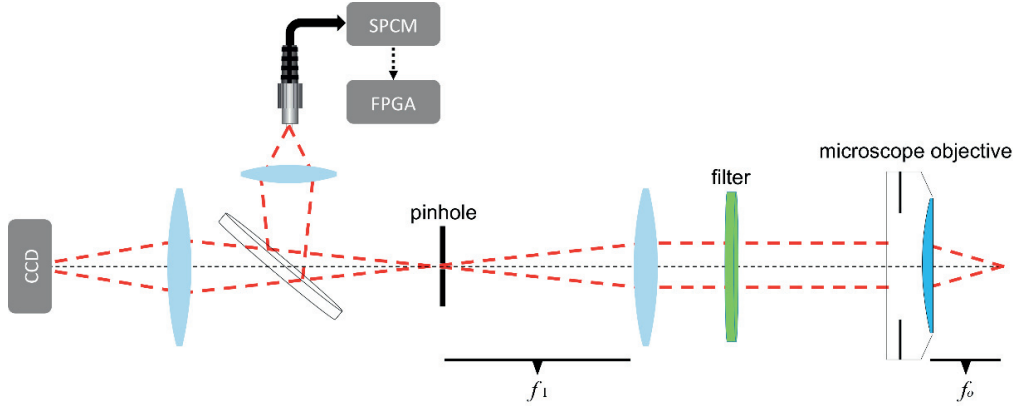
Figure 1.8: The optic train performing confocal detection of the fluorescent particle in the sample plane.

The fluorescence signal collected by the microscope objective passes through a bandpass filter and focused to the 1st image plane for further filtering (see **Figure 1.8**). The confocal detection of the fluorescence signal emitted from the target particle is managed through two optical components. One is the pinhole that selects a small area in the sample plane proportional to its size. The selected area with a pinhole of size r_p is $a = \pi \left(\frac{f_0 r_p}{f_1} \right)^2$. Furthermore, it rejects the off-plane auto fluorescence signal in the background, enhancing signal to the noise ratio. The second component filtering the environmental noise is fiber optic channel connected to the single photon counting module (SPCM). The signal survived in the optical fiber core and directed to the SPCM is limited to the NA of the fiber channel.

1.4.3 Kalman Filter

The Kalman filter [39] is one of the most popular algorithms extensively used in many different disciplines for information processing, estimation, and control. One of its famous applications was the spacecraft navigation for the Apollo project in 1960. Recently, it has been used for weather prediction [40], face recognition [41], curve fitting [42], and mobile robot localization [43]. The recursive nature of the algorithm makes it very powerful for real time applications. The information

from the past states are not necessary, so all the new data that is received is incorporated into the previous state. As the algorithm does not require mass computation and a storage unit for state history, it can operate at very high frequencies limited by the process time of recursive steps. The process time is reduced through a FPGA device where the computation, specific to the algorithm, is configured in a parallel manner that a conventional CPU architecture cannot provide.

In this work, a discrete Kalman filter is implemented to estimate the position of the particle subjected to Brownian motion. A pattern is fed into electro optic deflectors for scanning excitation in the sample plane. Then through fluorescence photons arrival times registered to the SPCM, the position of the molecule in the pattern is obtained. As the waist of the scanning laser beam has a finite size, these positions are not precise and so-called measured positions with a measurement noise. Moreover, since there is latency between the time positions are reported and the time physical feedback is applied, the main function of the filter is to estimate the correct feedback compensating the Brownian motion. A brief summary of the algorithm and optimization is shown below (see **Table 1.1**).

Predict	Update
mean: $x^- = \alpha_i x_{k-1} + \Lambda_k v_k + z_k$	mean: $x_k = x^- + g_k d_k$
covariance: $p^- = \alpha_i p_{k-1} \alpha_i^T + Z_k$	covariance: $p_k = cov(X_k - x_k)$

Table 1.1: Predict and update steps of a recursive Kalman filter.

x^- and p^- are prior estimates for mean and covariance of the state, respectively. x_k and p_k are the posterior estimates. The input transition matrix, the control matrix, and the input vector are given as α_i, Λ_k, and v_k. z_k is the process noise with a covariance of Z_k. The filter innovation is given as $d_k = m_k - \alpha_0 x^-$, where α_0 is the output transition matrix and $m_k = \alpha_0 X_k + w$ is the measurement matrix, including the noise w with a covariance of W. g_k is the critical term called "kalman gain" that minimizes the trace of the covariance matrix p_k. A simple derivation for the term is given below. The positions are measured directly, so in this task the transition matrices are $\alpha_0 = \alpha_i = I$.

$$p_k = cov(X_k - x^- - g_k(X_k + w - x^-))$$

$$p_k = cov((X_k - x^-)(I - g_k) - g_k w)$$

$$p_k = (I - g_k)cov(X_k - x^-)(I - g_k)^T - g_k cov(w)g_k^T$$

$$p_k = (I - g_k)p^-(I - g_k)^T - g_k W g_k^T$$

$$p_k = p^- - g_k p^- - p^- g_k^T + g_k(p^- - W)g_k^T$$

$$\partial tr(p_k)/\partial g_k = 2(g_k(p^- - W) - p^-) = 0$$

$$g_k = p^-(p^- - W)^{-1}$$

$$p_k = p_k(I - g_k)$$

As the position control is achieved through electrokinetic forces, the control matrix is $\Lambda_k = \mu_{ek}\Delta t$, where μ_{ek} is the mobility parameter and Δt is the time interval between two consecutive feedbacks. The main source of the process noise is the diffusion of the particle during consecutive updates; hence, $Z_k = D\Delta t$, and $z_k = 0$, where D is the diffusion constant. Given that the position is measured through a scanning laser beam, $W = \varphi/n$, where φ is a constant related to the beam geometry and n is the photon counts received for the given laser beam position. For instance, if we scan with a point-like beam and receive a high photon count, then the probability of the particle being at the position of the laser beam is the maximum; hence, the measurement noise converges to zero, $W \to 0$. Then X_k denotes the position of the laser beam controlled through the electro optic deflectors $X_k = X_{eod}$. The final parameters of the algorithm are given in **Table 1.2**.

Predict	Update $\{g_k = p^-(p^- - W)^{-1}\}$
mean: $x^- = x_{k-1} + \mu_{ek}\Delta t v_k$	mean: $x_k = x^- + g_k(X_{eod} - x^-)$
covariance: $p^- = p_{k-1} + D\Delta t$	covariance: $p_k = p^-(I - g_k)$

Table 1.2: Predict and update steps of the filter used in ABEL trap experiments.

2. Fluorescent Nanodiamonds in Biological and Biomedical Imaging and Sensing

This is a verbatim copy of a submitted book chapter to be published in Taylor & Francis: M. Kayci, F. Mor, & A. Radenovic. Fluorescent Nanodiamonds in Biological and Biomedical Imaging and Sensing.

2.1 Introduction

Fluorescent biomarkers, such as fluorescent proteins (FPs.) [44], organic dyes [45], and quantum dots (QDs) [46] have been widely used for biological and biomedical imaging due to their fair brightness and biocompatibility [47, 48]. However, these common fluorescent biomarkers have photobleaching, blinking or both properties that are not desired for bio-experiments. Therefore, recent efforts have been directed towards the development of a biocompatible luminescent or fluorescent labels that neither photobleach nor blink. In addition, higher molecular brightness in such ideal fluorescent probes would allow deeper and more sensitive fluorescence tomography. Fluorescent nanodiamonds (FNDs) present a good candidate for such ideal fluorescent probe since they are 5 to 100 nm in size [49], biocompatible with excellent photo-stability, and have a surface that can be easily functionalized [50]. These features have directed their use towards numerous demanding fluorescent imagining modalities, such as fluorescence lifetime imaging microscopy (FLIM) [51], fluorescence resonance energy transfer experiments (FRET) [52], long-term *in vivo* tracking [53], and stimulated emission depletion (STED) microscopy [54]. Moreover, the nitrogen vacancy NV centers in FNDs can act as optically readable sensors that could measure a variety of physical quantities with very high precision, including ultrasensitive magnetometery [55], sensing of the electrical fields [56], ion concentrations [57], and temperature [58]. From a biological point of view, it is extremely exciting to employ these nanoscale sensors in living cells as demonstrated by *Kucsko et al.* [58]. A recent work on a single NV center for single protein spectroscopy [59] paved way for future experiments in the cells, where the bulk diamond should be replaced by a nanodiamond with similar NV magnetic sensitivity.
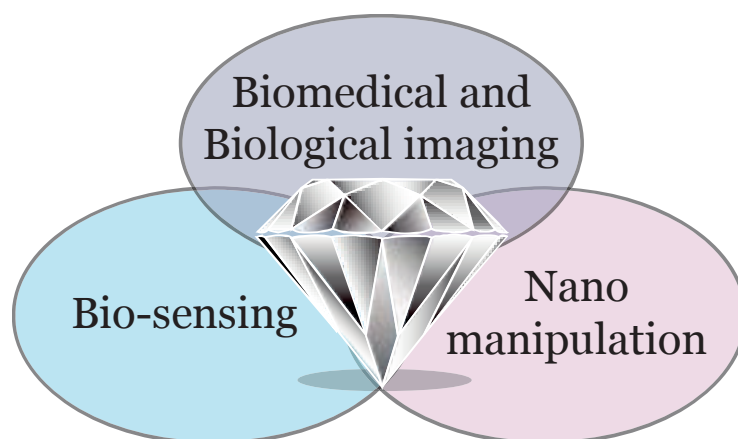
Figure 2.1: Fluorescent nanodiamonds are applied in numerous research fields. We have selected three areas that could potentially be of interest to life scientists.

In this chapter, the vast body of work will focus first on the physical properties and optical characterization of FNDs that could be of interest to life scientists. Next, we outline the applications of FNDs in bio-imaging and bio-sensing (**Figure 2.1**). Finally we show interesting applications using optical tweezers and microfluidics chips that allow three-dimensional (3D) nano-manipulation of these multipurpose probes. Three-dimensional nano-manipulation is an essential prerequisite for their use in closed microfluidic and intracellular environments.

2.2 General Properties of Fluorescent Nanodiamonds as Biomarkers and Biosensors

In the ideal case, the diamond is transparent, due to its large bandgap (5.5 eV); however, a presence of a defect can induce a level structure shortening of its band gap that is sufficient to permit the excitation in the visible spectrum (750 - 400 nm corresponding to .65 - 3.1 eV). If these defects are stable inside the crystal lattice, they perturb the energy level structure by introducing narrow levels within the bandgap.

If the defect transition energy is smaller than the band gap of the hosting diamond, then the emission from the defect will not be absorbed by the hosting material. As the resulting sharp zero phonon line (ZPL) transition has a specific location in the emission spectrum and the diamond acquires a characteristic color, the defect is the so-called color center. More than 500 color centers have been investigated in the wide band gap of the diamond, but only a few of them have been

identified as bright and stable [60]. The two most common centers are the neutral center, NV^0 and the negatively charged center, NV^-. Among these color centers, NV^- center is identified to be the most promising due to its spectral and spin properties compatible to applications ranging from quantum information processing to nanoscale metrology. NV^- center in diamond crystals is formed in C_{3v} symmetry by a nitrogen impurity adjacent to a carbon vacancy (shown in **Figure 2.2. a**).
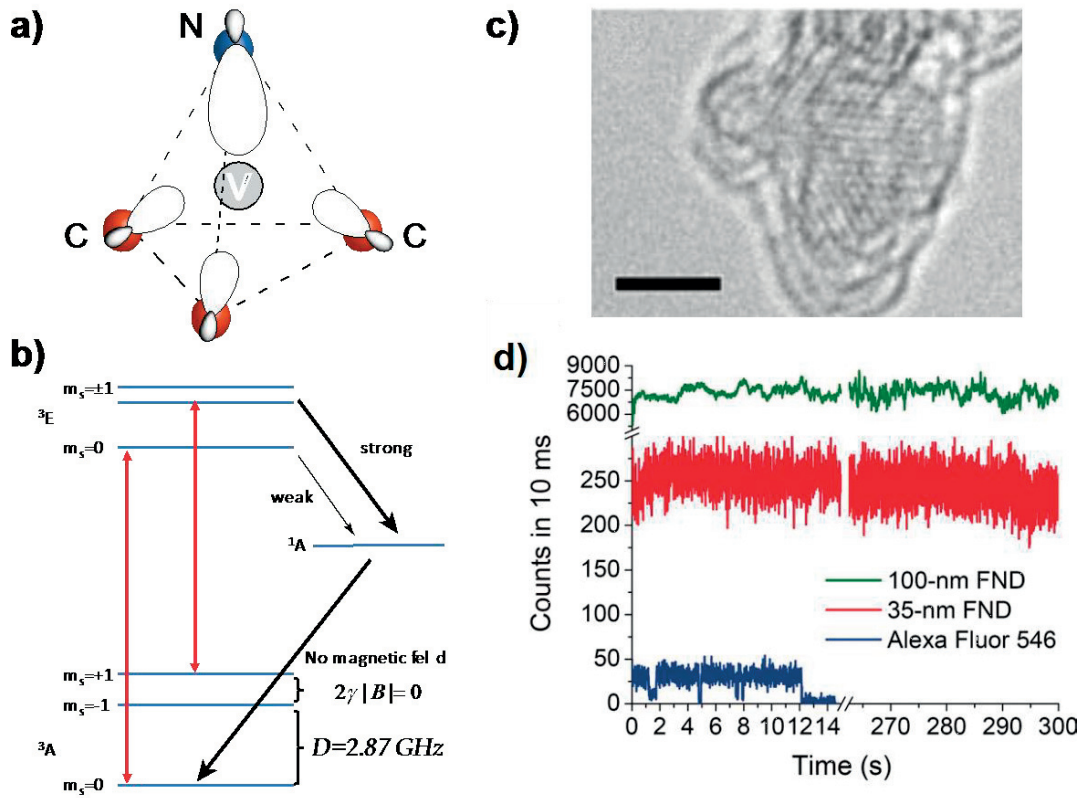
Figure 2.2: a) A crystal model of the single NV^- center (shown in grey) hosted in the diamond crystal lattice having a substitutional nitrogen (shown in blue) adjacent to a carbon vacancy. Image taken from [61]. **b)** Energy diagram of the ground state ^{3}A, excited state ^{3}E, and metastable singlet state ^{1}A represented for NV. Image taken from [61]. **c)** High-resolution TEM image of a 5 nm large nanodiamond revealing diamond (111) crystal planes. Scale bar: 2 nm. Reprinted with permission from [62]. **d)** Fluorescence time traces for a single 100-nm FND (green), a single 35-nm FND (red), and a single Alexa Fluor 546 dye (blue). To allow long-term observation, dye molecule are attached to a single dsDNA molecule, while FNDs were adhered to the glass coverslip. In the 300s time window, the fluorescence signal was stable with no observation of blinking or photo-bleaching for both sizes of FNDs. Reprinted with permission from [63].

These defects might occur in nature under high pressure and temperature conditions that occur in the protoplanetary disks of certain types of stars [64, 65] and also isolated and identified in the meteorites [66]. Similarly in artificial FNDs, NV centers are produced either under high pressure and

temperature or can be generated through electron and ion irradiations [67]. The irradiation damages in the diamond lattice can be annealed to diffuse the vacancies to the implanted nitrogen atoms. Recently, defect hosting in a FND as small as 5 nm has been synthesized [62, 68] (shown in **Figure 2.2. c**). This opens a gate for nanoscale drug delivery and real time monitoring of various physical quantities, such as temperature [69], pressure [70], magnetic field, and ionic concentrations [71] in a cellular environment.

A single NV$^-$ defect exhibits two level quantum system and as there is a short lag between the excitation and subsequent decay, it emits a photon at a time, which enables single photon applications. It has non-photo bleaching non-blinking stable fluorescence characteristics with a quantum yield close to unity at room temperature. In terms of bio-imaging, these unique properties are extremely useful. For example, broad fluorescence emission conveniently centered around 700 nm, guarantees negligible interference with cellular autofluorescence (see **Table 2.1)**. The fluorescence signal of these defects, hosted in NDs larger than 5 nm, is extremely stable devoid of blinking and photobleaching [55, 72]. Furthermore, it has been demonstrated that diamond nanocrystals hosting NV$^-$ defects are biologically inert and do not induce cytotoxicity and apoptosis in most tested cell lines [50, 73]. Yet, numerous functionalization protocols took advantage of either hydrophilic-oxygen terminated diamond surface or hydrogen terminated surface resulting in the applications where FNDs were coupled to proteins [74] and DNA molecules [75]. Recently, FNDs functionalization has been simplified exploiting silica encapsulation allowing better colloidal stability [76]. All the above-mentioned properties make FNDs a promising candidate for the next generation of biomarkers. In order to put into context the performance of this newly emerged biomarker, **Table 2.1.** lists literature reported values of fluorescent properties for single NV^{--}, quantum dot, typical organic dye, EGFP protein, and cellular proteins that give rise to auto-fluorescence. It is evident that single NV$^-$ center will outperform both quantum dots and EPGF protein cluster while cellular autofluorescence is an order of magnitude lower.

Property	NV⁻ defect in nanodiamond	Quantum dot [77]	Organic dye [77]	EGFP	Auto-fluorescence of protein clusters
Size	>4 nm [62, 78]	3-10 nm	<1 nm	~3 nm	>3 nm
Quantum yield	0.7-0.8	0.1-0.8	0.5-1	0.6	0.26 [79]
Lifetime	25 ns	10-100 ns	1-10 ns	1-4 ns [80]	NA
Molecular brightness	500-100 kcps	50-200 kcps	10-150 [81]	25 kcps [82]	2.1 kcps [82]
Bleaching	No	No	Yes	Yes	Yes
Blinking	No	Yes	Yes	Yes	Yes
Emission spectrum	680-800 nm	IR-UV selected by size	IR-UV selected by type	500-520 nm	250-650nm
Toxicity	Low	From low to high	Dye dependent	None	None
Thermal stability	High	High	Low	Low	Low

Table 2.1: Comparison of fluorescent properties for single NV⁻, quantum dot, typical organic dye, EGFP protein, and cellular proteins that give rise to cellular auto-fluorescence.

In addition to their use in imaging, NV⁻ defects hosted in FNDs are extensively employed in quantum computing due to their long spin coherence time [83], and optically addressable spin states [83]. At room temperature, NV center has a sharp ZPL, arising by zero-zero vibronic transitions, that is well resolved from the phonon side bands (PSBs), arising by phonon assisted transitions. The indistinguishable photons in the ZPL make it an outstanding emitter for quantum optics [84, 85].

The basic motivation behind NV⁻ centers as building block of the hardware for quantum computing is its high level control properties on a solid-state platform. Owing to its atom-like structure, NV⁻ defects are a promising alternative to trapped ions that are isolated from environmental couplings and hence offer high precision measurements [86]. While the isolation approach imposes special requirements (e.g. high vacuum, low temperature) on the environment and complicates integration stage and scaling up of the technology, the NV⁻ defects hosted in FNDs are capable of operating under ambient conditions. As single NV⁻ center has a nuclear spin with long coherence time, which

can be used as quantum register, and an electron spin, which can be used as a control or detection unit of nuclear spins, it has been intensely studied for the realization of quantum processors.

NV⁻ centers in FNDs have two unpaired electrons forming electron spin triplets, S=1, in the ground and excited states. Optic excitation operates as a pump for ms=0 sublevel of the ground state, ^{3}A. Given that ms=0 and degenerate sublevels ms=±1 are separated by zero field splitting parameter *D*, a resonant microwave signal will excite optically populated ms=0 state to the ms=±1 states at this frequency (as shown in **Figure 2.2.b**). As ms=±1 states have higher probability of going intersystem crossing (ISC), which leads to a decrease in the fluorescence, this mechanism serves as basis of optically detected magnetic resonance (ODMR). The ODMR spectrum of NV center is a powerful tool used in nanoscale sensing as it reflects local physical perturbations influencing the state transitions. It has been shown that the splitting parameter *D* is temperature [58] and pressure [70] dependent and that single NV center can be used as a sensitive nanoscale sensor (see **Table 2.2)**.

In the presence of a static magnetic field *B* aligned to NV center quantization axis, field ms=±1 degeneracy shifts by $\Delta = m_s \gamma B$, where γ is NV gyromagnetic ratio. When the field is not aligned, multiple centers in a single FND provide four resonance shifts in the ODMR spectrum with each for one crystallographic axis projection. Using this property, one can resolve vector magnetic field by a reference magnetic field fixed in orientation.

Physical quantities can also be resolved via pulsed ODMR spectroscopy, as single NV center can form an effective two-level quantum system. In Ramsey pulse sequence scheme, the phase acquired in the free precession time is proportional to the external magnetic field. Therefore, the spin dependent PL of NV center can be used for DC magnetometry [87]. Moreover, a spin echo pulse sequence synchronized to an AC field behaves phase additive on each half of the sequence, which can be used for AC magnetometery [88]. In such pulsed experiments, as the optic and microwave excitations are not performed simultaneously, the microwave excitation tuned down will reduce the power broadening and the optic excitation tuned up will increase the collected photons resulting in an enhancement in sensitivity compared to continuous wave excitation experiments.

High-spatial-resolution magnetic field detection cannot be performed in cell-like environments with methodologies such as SQUIDs [89], the Hall effect in semiconductors [90], atomic vapor based magnetometry [91], as well as magnetic resonance force microscopy [92]. Measurement of weak magnetic fields in biological samples with nanometer spatial resolution is thus an important problem to study. The possibility to detect such weak magnetic fields has become possible through

taking advantage of the above mentioned quantum properties of NV centers. As a sensor, NV centers are better suited to probe magnetic fields compared to electric fields, due to its moderate sensitivity to the applied electric field compared to quantum dots [56] (see **Table 2.2).** NV centers embedded in single FNDs make the measurement of magnetic fields possible with hundreds of nT Hz$^{-1/2}$ sensitivity due to the fact that the applied static or oscillating magnetic field causes the relative energy shift between two Zeeman sublevels. While, in the case of electric field sensing, the electric inaction caused by the Stark effect and spin orbit coupling is much weaker and reflected in lower sensitivity.

Researchers have shown the possibility to sensitively detect individual charges in 3D by the rotation of a magnetic bias field [56]. This methodology is designed around a quantum-metrology technique based on a single NV defect center spin in FND, which could reach a sensitivity of 202 V cm^{-1} Hz$^{-1/2}$. This is equivalent to a single elementary charge placed at a distance of ~ 150 nm from the FND particle probe and sensing NV spin within one second averaging was required. In addition, 100-s averaging was needed to sense a single electron charge from a distance of 35 nm with a signal-to-noise ratio of more than 1000. Similarly to magnetic field detection [87], the sensitivity on electric fields measurements is much better when performed with the field-induced phase accumulation method [56]. Increasing the evolution time, τ, from 8 to 80 μs allows a more precise determination of minimally detected electrical fields as small as 7 V cm^{-1}.

Temperature sensing at nanoscale and with high sensitivity is also possible using single defects in FND. The spatial resolution is related to the size of the FND, as in NSOM, whereas the sensitivity depends on the NV concentration [69]. The temperature noise floor that can be reached corresponds to 5 mK Hz$^{-1/2}$ for single defects in bulk sensors. In contrast, the temperature noise floor is 130 mK Hz$^{-1/2}$ with a precision down to 1 mK for nanocrystal sizes [93]. In consequence, temperature can be probed over length scales of a few tens of nanometers. The unique possibility to combine such accuracy and position resolution with the high photostability of FNDs should enable detection of heat produced by chemical reactions taking place among single molecules. In the absence of an external magnetic field, the temperature shifts the ground state electron spin polarization, $m_S = 0$ with respect to the sublevels $m_S = \pm 1$. Experimentally, this shift, referred to as axial ZFS, was found to vary significantly as of function of temperature [69]. To sense the temperature, one optically measures either the parameter D (~ 2.87 GHz) with the ODMR technique [69], which corresponds to the ZFS, or the ground state spin coherence time (~ 1 ms) [58, 94]. The principle of the latest method is to detect the NV fluorescence modulated with $\cos(2\pi\Delta D\tau)$, that is,

a D-Ramsey oscillation with frequency ΔD. Fluorescence as a function of evolution time provides an increasing phase accumulation, τ, and thereby improving the temperature uncertainty [58]. Increasing τ from 50 to 250 µs makes it possible to identify temperature variations as small as 1.8 mK in an ultrapure bulk diamond sample [58].

Property	Typical Sensitivity		Reference(s)
Pressure	6.8 bar √Hz	Via zero field splitting parameter D	[70]
Temperature	0.13K√Hz	Via zero field splitting parameter D	[69]
Magnetic field	0.36 µT/√Hz	Zeeman effect	[55, 88, 95]
Electric field	(ε_{xy}=280 ε_z 5.8) V cm^{-1}/√Hz	Stark effect and spin-orbit coupling	[56, 96]
Orientation	0.1°√Hz	Via zero field splitting parameter D	

Table 2.2: NV based sensor typical sensitivities adapted from [97].

2.3 Nanoscale Imaging of Biological Systems with NV-centers Hosted in Nanodiamonds

Due to their high photostability and biocompatibility, FNDs are well-suited far- and near-field probes for imaging purposes of intracellular environments with resolution below the diffraction limit. The first reported use of FNDs as biological markers for diffraction limited imaging dates back to 2005 when a team lead by Huan-Cheng Chang demonstrated that FNDs are spontaneously internalized in HeLa cells and display no cytotoxicity [50] (see **Figure 2.3. a).** Besides imaging, single particle tracking (SPT) techniques are instrumental when studying the bio-molecular activity occurring at the intracellular level. Shortly after, their application in fluorescence imaging, excellent photostability of FNDs has been exploited for long-term three-dimensional tracking of single 35 nm large FNDs in a living cell [49] (see **Figure 2.3 b).**
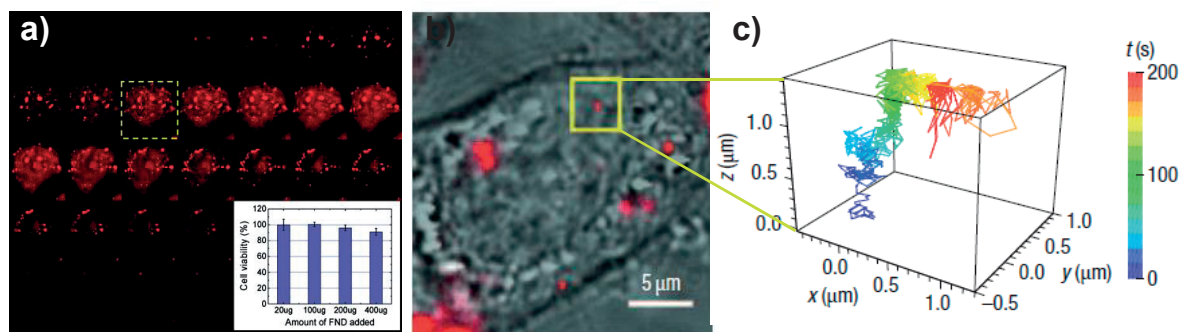
Figure 2.3: a) The cross-sectional confocal fluorescence images of a single 293T human kidney cell after FND uptake. Inset shows cell viability test demonstrating low cytotoxicity of FNDs. Reprinted with permission from [50]. **b)** Three-dimensional tracking of a single FND in the cytoplasm of a living cell. Merged bright-field image of the HeLa cell with the epifluorescence image of the single FNDs and FNDs agglomerates. **c)** 3D trajectory of the selected single FND particle (shown in b)). Single FND is followed for about 200 s as it diffuses through the cytoplasm. b) and c) adapted with permission from [49].

Chang et al. could track single FND for periods longer than 200 s. Since then the use of FNDs as biomarkers and as fluorescent probes for long-term tracking has exploded and now it is not only limited to the cells, but also includes organs and model organisms (including *C. elegans* [98], Drosophila [99], Mice [100], and Zebrafish [101]), which allows to study a wide range of biomedical problems, such as organ development [51], embryogenesis [99], stem cell proliferation [51], neuronal survival and morphogenesis [102], and cancer cell identification [103]. In addition, FNDs as biomarkers have opened the door to novel imaging and SPT modalities that are not accessible to conventional fluorescence microscopy, including orientation tracking over long periods, with resolution in the millisecond timescale of intracellular events [104]. In biomedical imaging, NDs are used as contrast agents in magnetic resonance imaging (MRI) [105].

2.4 Super-resolution Microscopy with Fluorescent Nanodiamonds

The past decade has been marked with the rapid progress in super-resolution microscopy. Methods based on localization and tracking of single-particle light emitters are required for applications ranging from high-resolution optical microscopy and bio-sensing to single molecule detection [106]. Even though fluorescent proteins and organic dyes are standard probes in the domain of super-resolution localization microscopy, nanosized photoluminescent probes with efficient linear and nonlinear optical response, including FNDs [107, 108], ferroelectric perovskites [109-112], and upconverters [113] are attracting researcher's attention. Although all these kinds of particle-probes

are by its virtue highly photostable and low-power laser excitation, with the possibility to obtain FNDs smaller than fluorescent proteins [66] makes them the most suited labelling candidates to circumvent the diffraction resolution barrier down to a few nanometers. Near-field scanning optical microscopy (NSOM) of soft biological structures and the detection of molecular interactions became possible after the advent of AFM and force spectroscopy techniques. Essentially, NSOM presents the first nanoscopy imaging technique and it exploits the evanescent field produced by a subwavelength aperture. In 1928, Edward H. Synge (1890-1957) proposed the original idea for NSOM; however, it took more than 50 years to experimentally realize this idea requiring a technological progress development of lasers, microfabrication of subwavelength apertures, precision positioners, single-photon detectors, and computers [114-116].
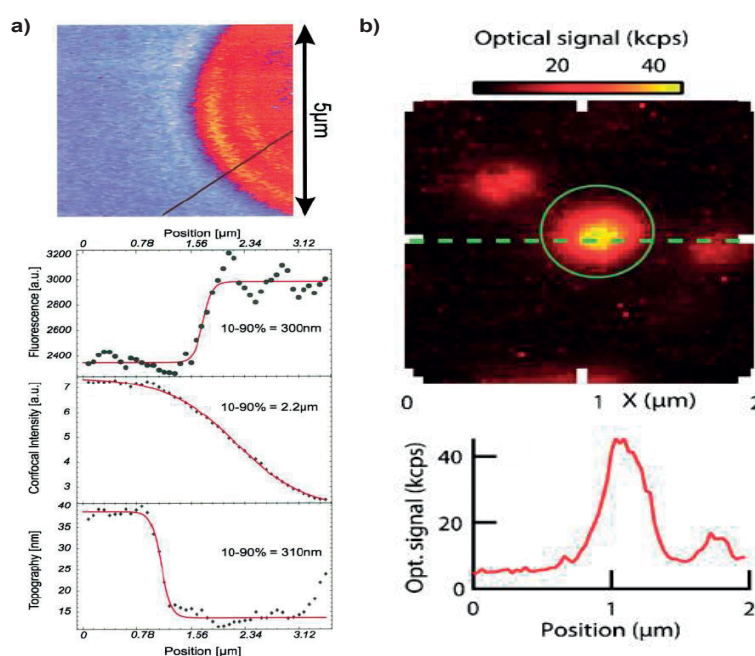

Figure 2.4: a) First NSOM scan taken with the fluorescence nanodiamond attached to the tip. The scan is taken in a constant-gap mode across a section of a gold mask. Adapted with permission from [108]. **b)** Luminescence image of a single FND. The image is recorded at an excitation optical power of 100µW measured at the tip apex. Corresponding optical cross-section. Adapted with permission from [117].

Interestingly, the resolution in NSOM, which allows for simultaneous high-resolution measurements of topology and fluorescence, is not limited by light diffraction, but by the size of the scanning probe, which is composed by a tapered optical fiber having a diameter of ~ 50 nm. Inspired by scanning optical microscopy, it has been reported that a single FND can be attached to a NSOM tip and used as a local light source [108]. Excitation of the FND crystal at the end of the tip was performed using an illumination light waveguided through the fiber holding it. The NSOM images taken with the FND crystals as a light source of a gold mask in fluorescence mode showed, however, a resolution of only 300 nm shown in **Figure 2.4. a**. To further increase the resolution, it was proposed to implement

tips with smaller crystals with a single colour center [108]. Significant improvement in resolution has been achieved by using much smaller FNDs of 25 nm. **Figure 2.4 b,** demonstrates that NSOM can detect nonbleaching luminescence signal from an individual FND hosting a single NV color center [117]. Here, reported FND was smaller than 25nm in diameter. Another possibility to overcome the diffraction limit is to exploit the effect of stimulated emission discovered by A. Einstein [118], and subsequently demonstrated experimentally by S. Hell [119, 120].

In brief, STED microscopy is a far-field approach that takes advantage of the limitations of matter to be imaged in order to reconstruct a super-resolution image. Stimulated emission is a physical process where an excited atomic electron, or an excited molecular state, may drop to a lower energy level transferring its energy to an electromagnetic wave of a certain wavelength. In addition to the excitation laser, a second-laser, referred to as STED laser, cancels fluorescence of the emitter located outside the center of excitation.

Technically, the doughnut-shape de-excitation STED laser is realized with a phase modulator. STED microscopy was used to image NV centers with nanoscale resolution and using focused laser light [107]. Only the NV centers hosted in FND that are located in the subdiffraction-sized area around the doughnut, where the STED beam intensity is lower than the threshold of the excited state depletion by stimulated emission, are not turned off and therefore still allowed to emit and to be identified among multiple centers present in 50-100 nm large FND (see **Figure 2.5)**.

To achieve such performances, the intensity of the STED laser, I_{STED}, has to be in the order of GW cm^{-2} pointing that only robust markers can be used. In case of highly photostable FNDs, application of I_{STED} = 3.7 GW cm^{-2} was needed to reduce the focal spot, i.e. FWHM, from 223 nm in diameter down to 8 nm [107] as shown in **Figure 2.5 a-c**. Further increasing I_{STED} up to 8.6 GW cm^{-2}, compresses the FWHM to values as small as 5.8 nm in 1D, which is still predicted by the theoretical inverse square-root law [121]. This value is 133 times smaller than the used wavelength for imaging the colour centers in single FNDs and represents a new regime in optical-based microscopy. Recently, up to 5 single NV cementers have been resolved from the single FND using super-resolving STED microscopy [122] **Figure 2.5 d-e.**
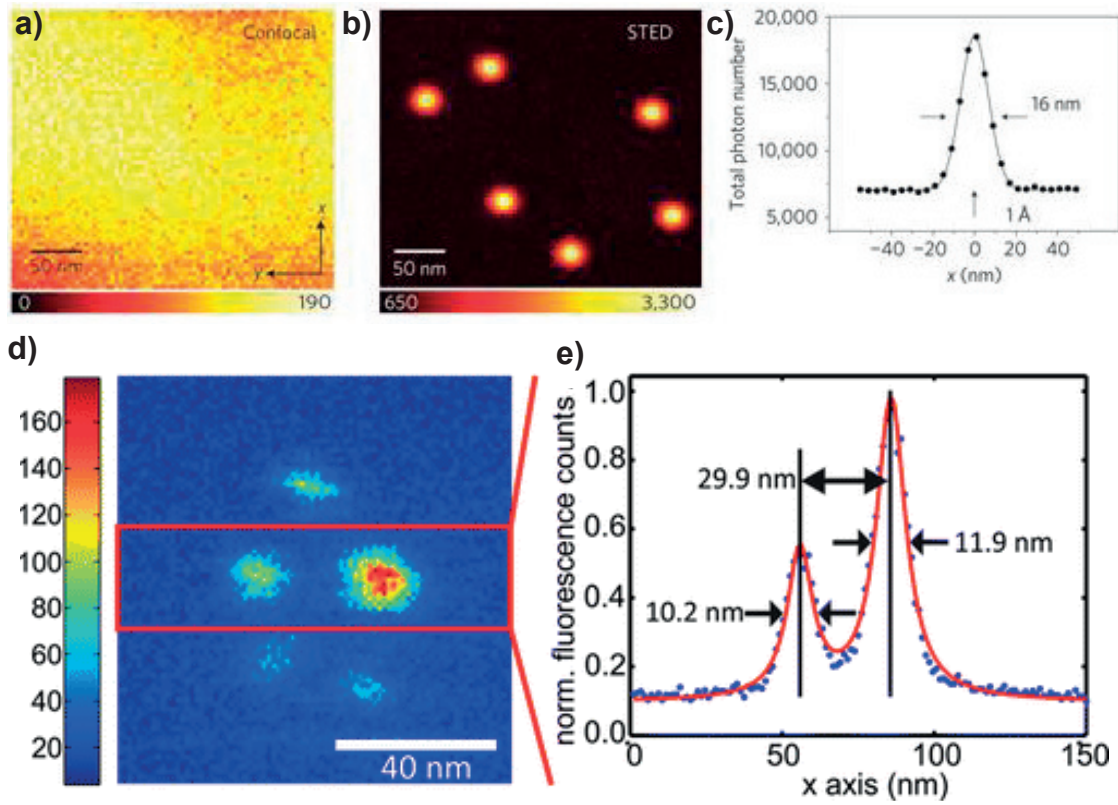
Figure 2.5: a) Conventional confocal microscopy image, which displays a featureless image, while in **b)** the super-resolving STED microscopy image reveals individual luminescent NV centers inside the diamond crystal. **c)** Corresponding vertically binned STED image profile showing one NV center. Figures a) b) and c) were adapted with permission from [107]. **d)** Subdiffraction resolution STED image of single FND hosting 5 NV centers and **e)** corresponding vertically binned STED image profile. Figures d) and e) were reprinted with permission from [122].

Manipulation of spin degrees of freedom using conventional far-field optical microscopy techniques is limited by diffraction. In principle, one cannot resolve spins by less than 250 nm. In contrast, the spin- reversible saturable optical linear fluorescence transitions (RESOLFT) microscopy, developed specifically for far-field imaging and manipulation of individual NV electronic spins in FND, revealed a nanoscale resolution [123].

Figure 2.6: a) Experimental sequence of spin-RESOLFT. NV spins are first optically pumped to ms=0 with a Gaussian beam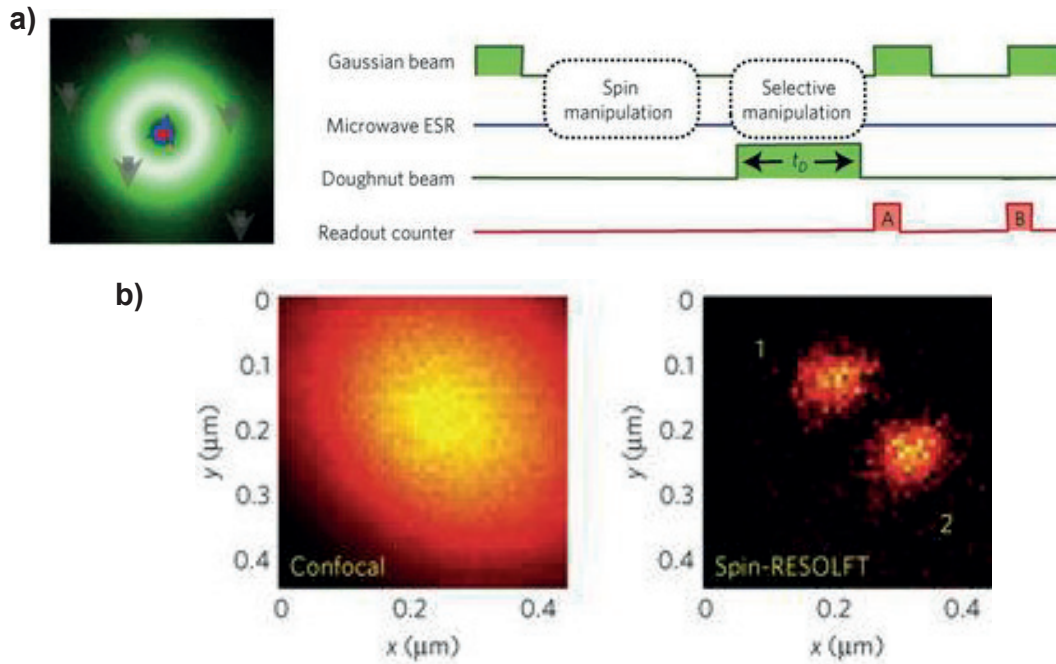 at 532 nm followed by microwave manipulation. Application of a 532 nm doughnut beam repolarizes the outer ring to ms=0, which allow the spin state of the central dark region to be independently read-out. **b)** In the confocal (image left), it is not possible to multiple NV⁻ centres, whereas 2D spin imaging using spin-RESOLFT (image right) clearly resolves two NV centres separated by ~150 nm. Reprinted with permission from [123].

The basic idea in the spin-RESOLFT approach for spin detection and control with subdiffraction resolution is shown in **Figure 2.6 a**: (i) to polarize by optical pumping a NV center, (ii) coherently manipulate the NV center with resonant microwave and (iii) detect its spin-state-dependent fluorescence [123]. To improve the spatial resolution, the sample is illuminated with a doughnut-shaped laser beam, as in STED microscopy, just before reading the spin state. In consequence, spins that are not in the center of the doughnut contribute differently to the fluorescence signal compared to spins located at a few nanometers from the center of the beam. Using the spin-RESOLFT technique applied to an NV center in the diamond, it is possible to optically image a single spin with a resolution down to 38 nm employing only 2-mW total doughnut beam power focused to a diffraction-limited spot of 0.07 µm² [123]. The resulting intensity corresponds to ~ 3 MW cm⁻², and can be further reduced by a factor of 20 while keeping a similar resolution by increasing the duration of the doughnut pulse, t_D, from 12.5 to 100 µs [123]. Compared to STED, the spin-RESOLFT

microscopy technique needs 4 orders of magnitude less power for comparable resolution [107]. It is also interesting to note that the length of t_D is limited by the spin-state relaxation time (> 100 ms) and the electronic excited-state lifetime (~ 10 ns) [123].

On one hand, we have deterministic super-resolution imaging techniques, such as STED and spin-RESOLFT, which are capable of resolving NV centers down to 5.8 nm and 38 nm, respectively [107, 123]. However, these approaches require either a high power density for the doughnut-shaped depletion beam (~ 1GW cm^{-2}) [107], or due to the serial scanning measurement results in a slow frame rate [123], leads to the problematic imaging of dynamic processes in living cells.

Stochastic super-resolution imaging techniques, such as PALM [124, 125] and STORM [126], which are based on the localization of sequentially activated photo-switchable fluorophores, are better suited for fast image acquisition. However, they are affected, among others, by the precise localization of stochastic switching events and the compromise between bleaching and imaging rate. In consequence, the search of fast and noninvasive non-scanning imaging techniques with sub-diffraction resolution and accuracy continue. In contrast to PALM and STORM, the wide-field super-resolution microscopy using spin-dependent fluorescence in nanodiamonds, referred to as deterministic emitter switch microscopy (DESM), demonstrated the capability to image a 35 x 35 µm^2 surface composed by 100 NV centers in FNDs with a localization precision between 12 and 46 nm, and employing only 90 s [127]. In DESM, the principle is to exploit the dependence of the fluorescence intensity of the NV centers as a function of the spin orientation. In this context, the ODMR technique allows to measure the spin resonance frequencies of all centers within a diffraction-limited spot. If the centers do not overlap, one can distinguish them by microwave excitation in a deterministic way. In consequence, this methodology works properly while FNDs are arbitrarily oriented leading to multiple spin transitions. The basic procedure in DESM to achieve a sub-diffraction resolution is to resonantly drive only one ground-state spin transition at a time [127]. Up to now, the world record in far-field based super-resolution optical microscopy, i.e. 8 nm in 2D and 5.8 nm 1D, is held by NV centers embedded in single FNDs [107].

2.5 Nanoscale Sensing of Biological Systems with NV centers Hosted in Nanodiamonds

As introduced in the section related to sensing properties of NV centers hosted in FNDs, various physical properties can be detected with high accuracy. Here, we detail the two most prominent examples related to biological systems.

So far, temperature measurements of biological environments at nanoscale resolution presented a grand challenge in metrology. However, using the NV centers hosted in FNDs, according to *Kucsko et al.,* demonstrate nanoscale temperature probing of the interior of single human embryonic fibroblasts [58]. By inserting FNDs into single living cells, the FNDs were then irradiated with microwaves in order to modulate the electron occupancy of spin states. To determine the changes in the ground-state energy gap, authors used wide field fluorescence measurements that allowed to probe the temperature variations (the microwave frequency that corresponds to the energy difference between spin states) for several FNDs. The temperature inside the living cell has been also modulated by irradiating and heating the gold nanoparticles in the cell (see **Figure 2.7 a.** and **Figure 2.7 b).** Although most of the exciting applications of FNDs are related to fluorescence-based microscopy, especially in biology, where room-temperature functionality and chemistry are crucial parameters, another interesting sensing area is 3D MRI with NV centers hosted in diamonds.

In principle, a 1 nm resolution of single electron spins in a solid has been demonstrated [95], while a resolution of 400 nm has been achieved for living cells [128]. In contrast, in medical facilities and for biological tissues, the resolution for conventional MRI apparatus is about 1 mm, which demonstrates the huge potential for 3D MRI with NV centers hosted in diamonds. The most prominent example of the magnetic imaging on biological samples has been demonstrated using the magnetic field imaging array consisting of a nanoscale layer of nitrogen–vacancy color centers implanted on the surface of a diamond chip. *Le Sage* et al. have succeeded to localize magnetic nanoparticles (magnetosomes) produced in the magnetotactic bacteria (MTB) with sub-cellular spatial resolution (see **Figure 2.7 c.** and **Figure 2.7 d.)** [128]. Authors suggest that their method can be used to identify potential vertebrate magnetoreceptor cells [129], which should have a magnetic moment that is comparable to or larger than one found in MTBs.
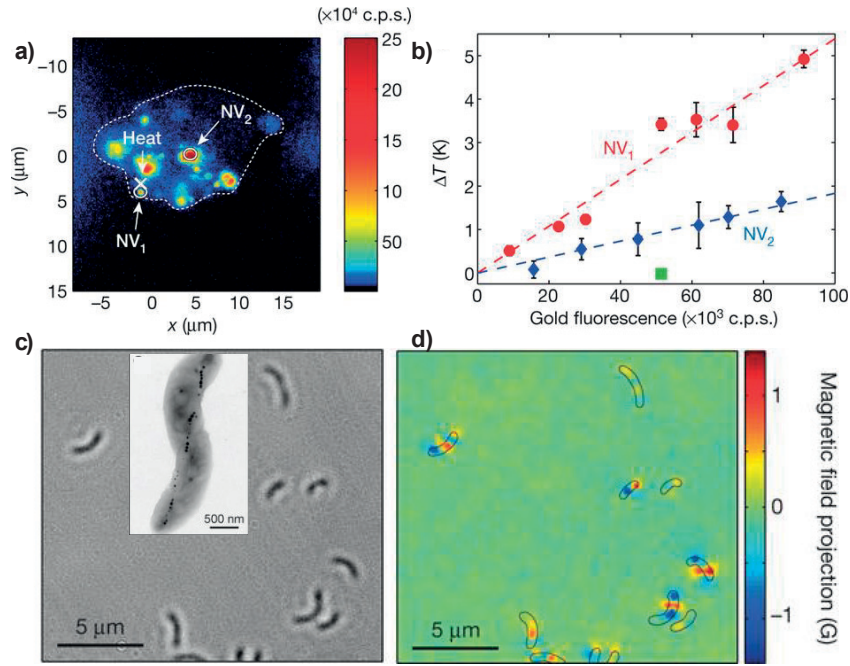
Figure 2.7: a) Confocal scan of a single living cell obtained using a laser excitation set to 532 nm, with a collection at wavelengths greater than 638 nm, which ensures collection of PL signal mostly from FNDs. The cross mark indicates the position of the gold nanoparticle used for heating, and the circles represent the location of the FNDs (NV$_1$ and NV$_2$) used for thermometry. Color bars indicate the fluorescence in counts per seconds. **b)** Measured temperature change at the positions of NV$_1$ and NV$_2$ relative to the incident laser power were applied to the gold nanoparticle. (a,b) Reprinted with permission from [58]. **c).** Wide-field optical image of dried MTB on a diamond chip. Inset shows a typical transmission electron microscope (TEM) image of a single MTB. Dark spots inside MTB are magnetite nanoparticles**. d)** Stray field distribution recorded with a wide-field NV magnetometer –imaged region corresponds to the one shown in c). (c,d) Reprinted with permission from [128].

2.6 Manipulation Techniques

In order to apply the full FND sensing in nanoscience and biology, the sensing probe in the form of the single FND, has to be positioned and manipulated with high accuracy over the sample. Several exiting techniques, such as scanning probe techniques, optical tweezers, and ABEL trap have reached required precision.

2.6.1 Scanning Probe

Due to its electronic and optic properties, a single NV center embedded in a FND can be attached to a probe tip, i.e. AFM, for atomic scale resolution in imaging, as shown in **Figure 2.8.** The idea is to bring the scanning probe close to the substrate surface and detect the local fields emanating from

the sample through the change in the spin dynamics. The spin dependent PL of NV center can be collected via far field optics, whereas optic and microwave excitations are realized in ensemble level. Alternatively, a fiber optic waveguide, serving as scanning probe that can be functionalized such that it delivers microwave signal through an integrated transmission line, performs optic excitation and collects the fluorescence simultaneously [130, 131]. Recently, an engineered NV center hosted in a scanning nanopillar waveguide with long coherence time (~75µs) and collection efficiency was shown to be a sensitive robust magnetometer imaging magnetic structures as small as 25 nm (see **Figure 2.8 d**.) [132].
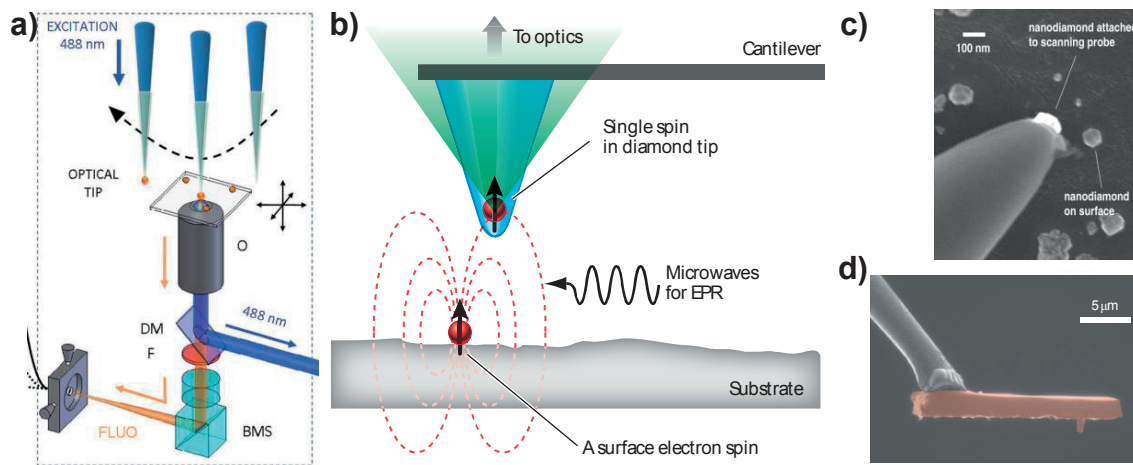

Figure 2.8: Scanning probe based FND manipulation techniques **a)** In the near-field scanning optical microscopy (NSOM/SNOM) FND has to be first picked by an optical fiber and then is scanned over the magnetic nanostructure. Reprinted with permission from [130]. **b)** Depicts basic principle of all scanning magnetometery techniques. In AFM, a sharp tip with a nitrogen vacancy center at the tip maps out the three-dimensional magnetic field vector above a magnetic nanostructure. Reprinted with permission from [133]. Several methods have been developed in order to position/fabricate the FND on the cantilever tip. **c)** FND can be picked up from the surface and attached to the cantilever tip. Reprinted with permission from [133]. **d)** Alternatively**,** diamond nanopillar probe with a single NV center in its tip can be fabricated from of a single crystalline as shown in SEM image Reprinted with permission from [132] .

Similar to the conventional MRI technique, the scanning probe tip can also be employed for the generation of a magnetic field gradient on NV centers [55]. This modality basically aims to detect the resonance ring of each NV center that appears by scanning the corresponding magnetic field under a fixed microwave excitation. Given the probe position, the gradient profile is known, and the NV centers can be localized with the ultimate resolution limited by the resonant ring width.

Recently, a spatial resolution of 9 nm has been demonstrated for proximal NV centers in clustered form. In all scanning configurations the optic data acquired by NV center can be easily correlated to topography mapping achieved with the probe tip for further enhancement in the imaging.

2.6.2 Optical Tweezers

Although the integration of single NV center to a scanning probe tip remarkably improved resolution, this approach has some drawbacks regarding experimental realization and operating environment. Firstly, to sense the local fields with high spatial resolution, the NV center should be placed close to the probe tip that requires nanoscale positioning and expensive fabrication process. Consequently, a significant effort has been put into the engineering NV defects in the diamond. Recently, stable NV centers as close as 2 nm to the diamond surface have been formed without degrading spin coherence time [134]. Yet, this limit is far beyond realization for the FND integrated to a scanning probe. Also, the probe tip may perturb the environment or the intrinsic characteristics of NV center. Moreover, as this approach is limited by operating environment of the probe tip, it is not a practical solution for closed microfluidics and bio-applications. Recently, optic-based trapping has been demonstrated as a nanoscale positioning tool for FND hosting NV centers [135] see **Figure 2.9. a**. This technique uses a piezoelectric stage performing 3D scanning of the sample with respect to the focused infrared beam where multiple FNDs are trapped through the radiation pressure. A second green laser optically excites the NV centers in FNDs, while the microwave signal is applied through a nearby antenna. Although the large ensembles of NV centers are randomly oriented in such trap environment, it is shown that the local DC magnetic field sensing is possible. Moreover, a recent work using counter propagating dual beam technique has achieved the trapping at single particle level [136] **Figure 2.9. b**. It is also shown that the orientation of the polarized beam on asymmetric nanodiamond can provide the control over the angle between the optic axis and the NV quantization axis with high accuracy. This progress facilitates three-dimensional directional magnetometer in solution.
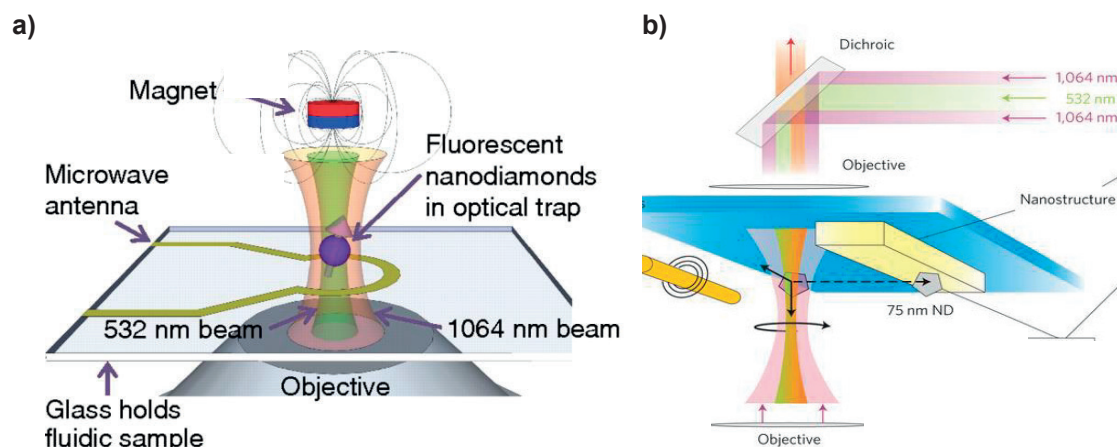
Figure 2.9: Two configurations base on 3D optical trapping optical trapping of FNDs that allow for manipulation of a single electron spin. **a)** Single beam optical tweezers, photoexcitation, and luminescence detection are integrated on the same setup using a High NA objective. The magnetic field is applied externally, along the axis of the objective. Reprinted with permission from [135]. **b)** The dual beam optical tweezers permits accurate control over the FNDs orientation. Reprinted with permission from [136].

2.6.3 ABEL Trap

Despite the fact that laser based trap is an outstanding manipulation tool for aqueous environments, it is not functional for FNDs of smaller sizes. Given that the force generated in optic tweezers is proportional to the volume of the trapped object, particles smaller than 100 nm requires high optic powers (~150 mW) [137]. This is not desirable in biological environments as it may affect the properties of the trapped particle, as well as the medium. Moreover, as the force arises through a second order interaction, the applied field must first polarize the object, and then generate the force between the induced dipole and a gradient in the field. The ABEL trap is a novel approach to overcome size limitations in a solution phase trapping.

It combines laser guided single particle tracking with a real time feedback, which cancels the Brownian motion. Unlike optic tweezers, the trap force is not optic based, but electrokinetic which scales linearly with the particle radius. Recently, single dye molecule of sub-nanometer size has been successfully trapped by a very low optic excitation power used in the particle tracking [138]. As the trajectories of diffusing particles are not correlated; thus, only one is exposed to the correct feedback, exactly one particle is trapped with this method. Moreover, all surrounding particles around the trap point are subjected to the same feedback, therefore applied electrokinetic force on

native environment is not perturbative **see Figure 2.10**. This also avoids any potential clustering or agglomeration that might occur in optic tweezers for dense dispersions.
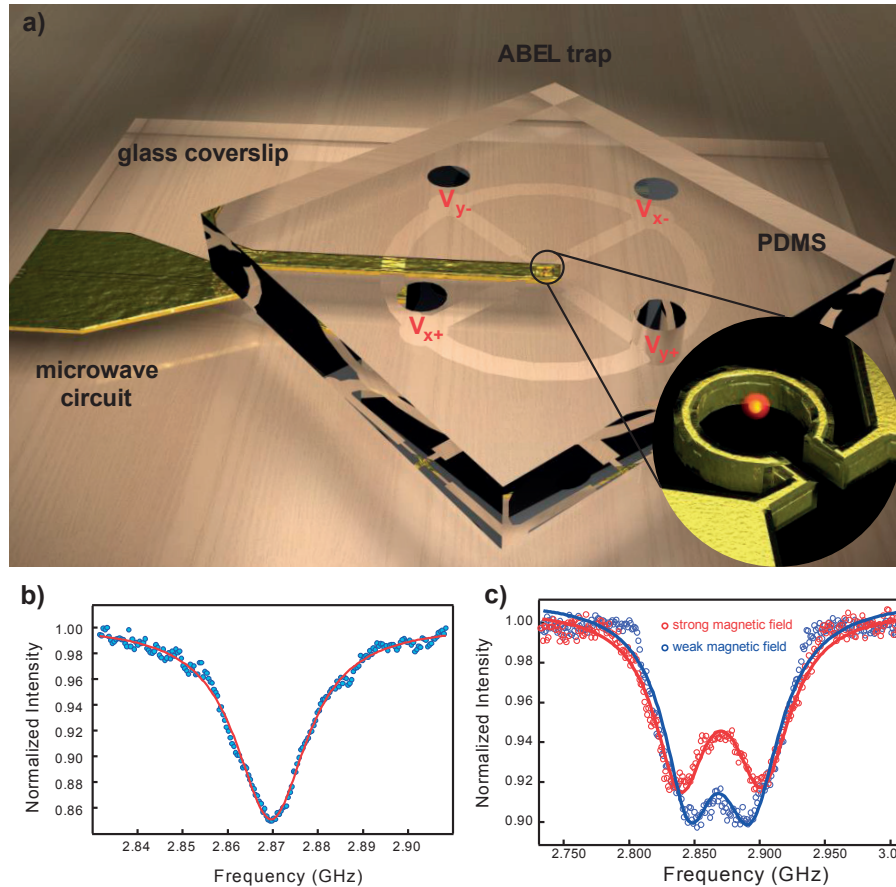
Figure 2.10: a) Schematic of ABEL trap PDMS microfluidic cell with RF circuit integrated on the glass coverslip. Inset show a zoom in the trapping area and it indicates the relative location of FND in respect to the area with the enhanced homogeneous magnetic flux density. **b)** Typical ODMR spectra of NV defects in ABEL trapped FND. b) Optically detected ESR spectra of an ABEL trapped single FND under presence of the weak and strong static magnetic field. Image taken from [61].

Provided that these advantages ABEL trap is an outstanding tool for FND manipulation and positioning. Indeed, more recently this approach has been validated with electron spin resonance experiments on 30 nm sized FND containing NV centers [61]. Although the particle has rotationally free behavior, the detection of static magnetic fields through the ODMR spectra has been demonstrated [61].

Moreover, a work by *Maclaurin et al.* [139] on single diffusing diamond nanocrystal shows the capability of the ABEL trap approach for sensing also the fluctuating and oscillating magnetic fields. As well as being a sensitive magnetometer, ABEL trap is compatible to other NV center based

detection schemes, such as thermometry and ion concentration measurements. With the advances in fabrication of stable FNDs, this technique will provide a new valley for three-dimensional high resolution imaging and sensing in fluidics and physiological environment.

2.7 Conclusion

With this chapter we attempted to give a short overview of the emerging new probes in the form of FNDs. We focused on their use in nanoscale imaging of biological samples and biological relevant sensing application, such as single cell thermometry and magnetometery. In relation to the sensing we have also reviewed current nanoscale manipulation techniques that would allow in the future positioning of these ultrasensitive sensors within a single living cell.

3. Single Fluorescent Nanodiamond in a Three-Dimensional ABEL Trap

3.1 Abstract

Three-dimensional single particle trapping and manipulation is an outstanding challenge in various fields ranging from basic physics to life sciences. By monitoring the response of a trapped particle to a designed environment, one can extract its characteristics. In addition, quantum dynamics of a spatially scanned well-known particle can provide environmental information. Precise tracking and positioning of such a particle in an aqueous environment is a crucial task for achieving nanoscale resolution. Here we experimentally demonstrate three-dimensional ABEL trap operating at a high frequency by employing a hybrid approach in particle tracking. The particle location in the transverse plane is detected via a scanning laser beam, while the axial position is determined by defocused imaging. The scanning of the trapped particle is accomplished through a nanopositioning stage integrated to the trap platform.

3.2 Introduction

Single particle trapping and manipulation can provide inner dynamics of single molecules that are not resolvable in ensemble level averaging measurements. Optical trap is one of the most powerful techniques that has been used for nanoscale positioning in biophysics and quantum optics. Recently, it has also been proposed as a three-dimensional scanning tool for nitrogen vacancy embedded single nanocrystal employed in quantum sensing [140]. However, this technique is not practical for particles smaller in size since the optic forces required for stable 3D trapping are proportional to the particle's volume. High optic powers on such particles may introduce heating that could perturb the biological environment [141]. Moreover, as any particles near the beam focus are subjected to the trapping forces, it is not selective. Therefore, single particle level trapping requires extremely low concentration, which is not the case for very crowded physiological environments. Instead, electromagnetic tweezers [142] can provide single particle selectivity since

they operate by active feedback control. However, the trapping is limited to magnetic beads and high driving currents on electromagnets could result in a substantial heating, which in turn requires an active cooling system. Less common, modalities such as dielectrophoresis [143], acoustophoresis [144], and Paul trapping [145] have also been used in single particle experiments, but unfortunately, all these techniques have constraints either related to the trapping environment or trapped particle characteristics.

ABEL trap is a promising technique that can overcome size limitations, as well as the environmental issues. It combines a very fast detection scheme with a real time feedback, which compensates the Brownian motion. Unlike optical or magnetic tweezers, the electrokinetic forces applied in ABEL trap scale linearly with the particle's radius. A single dye molecule of sub-nanometer size trapping has been achieved with a very low optical excitation used in the position tracking [138]. Given that the Brownian trajectories of multiple particles in the trap area are uncorrelated, only one is subjected to the correct feedback, hence exactly one is trapped during this process. Also, as all particles are exposed to the same feedback, the electrokinetic force on the environment is non-perturbative. The instant feedback does not generate a potential well in the trap area, but a uniform field directing the particle. This also avoids any clustering and agglomeration that occurs in passive trapping approaches when working with dense dispersions. Providing both electroosmotic and electrophoretic actuations, the trapping is not limited by dielectric, magnetic or charge properties of the particle. Therefore, any traceable particle can be trapped.

Although a two dimensional ABEL trap can provide precise measurements without physical perturbations like surface tethering [146] or excessive heating [141], the confinement in axial dimension by the geometry of trapping cavity may introduce undesired interactions. As the cavity depth used for confinement is very small and nanoscale particles have a very high diffusion coefficient, during a trapping experiment, such particles will have a very high surface collision rate. For instance, Rhodamine B in a cavity of 800 nm depth collides to the wall with 87 kHz frequency [147]. This interference may induce fluorescence quenching or absorption of the particle limiting the trap period and measurement precision. Improvement on microfluidics material and modification of the surface chemistry [148] has been proposed to remove such effects, but it requires complex fabrication process and is has a high cost [149]. Alternatively, a three-dimensional ABEL trap can provide collision free manipulation without the engineering of the chemical and the geometric properties of the cavity. Indeed, a recent work has utilized sets of micro electrodes patterned on two fused silica layers forming the trap chamber to achieve three-dimensional control

over the particle whose positon is detected by a CCD camera [150]. However, the close configuration of the electrodes in the trap chamber degrades the trap performance when a contamination process screens the applied voltages. Furthermore, video based position detection employed for all dimensions extends the feedback latency that plays a critical role in the trap resolution. Here we demonstrate soft lithography based microfluidics exploiting both electroosmotic and electrophoretic forces through electrodes inserted to the ports distant to the trapping chamber. To preserve high feedback frequency achieved in conventional laser guided 2D ABEL trap, we employed laser guided in-plane transverse detection scheme, while independently running image processing that estimates the axial position. With the presented approach, we extend the operating environment of the nitrogen vacancy (NV) defects hosted in FND from 2D to 3D, which opens the possibility for the use of NV based sensing and imaging applications in physiological environments.

3.3 Microfluidic Cell

Connected micro channels forming the microfluidics provide the interface between the physical voltages on the electrodes and the trap chamber. The forces introduced by the microfluidics are the main control units correcting the position of the particle. In our 3D microfluidics trap, both electrophoretic and electroosmotic forces are contributing to the electrokinetic mobility due to the converging electric field on the trapped particle and long micro channels in which mobile ions are generating bulk flow.

The microfluidics in PDMS (polydimethylsiloxane), providing the transverse plane position control, was fabricated using multilayer SU8 masters (for details see **Supporting Information**). The trap chamber in the center was formed by precisely punching the intersection of the channels each responsible for one-dimensional control. Then, a second microfluidic layer was cascaded in such a way that a new channel connected to the chamber introduced the position control in the axial dimension (see **Supporting Information**). Besides the simple integration of insertable electrodes, this configuration also provides the control over the full axial chamber size that is very helpful in suppressing the background fluorescence noise (**Figure 3.1**).
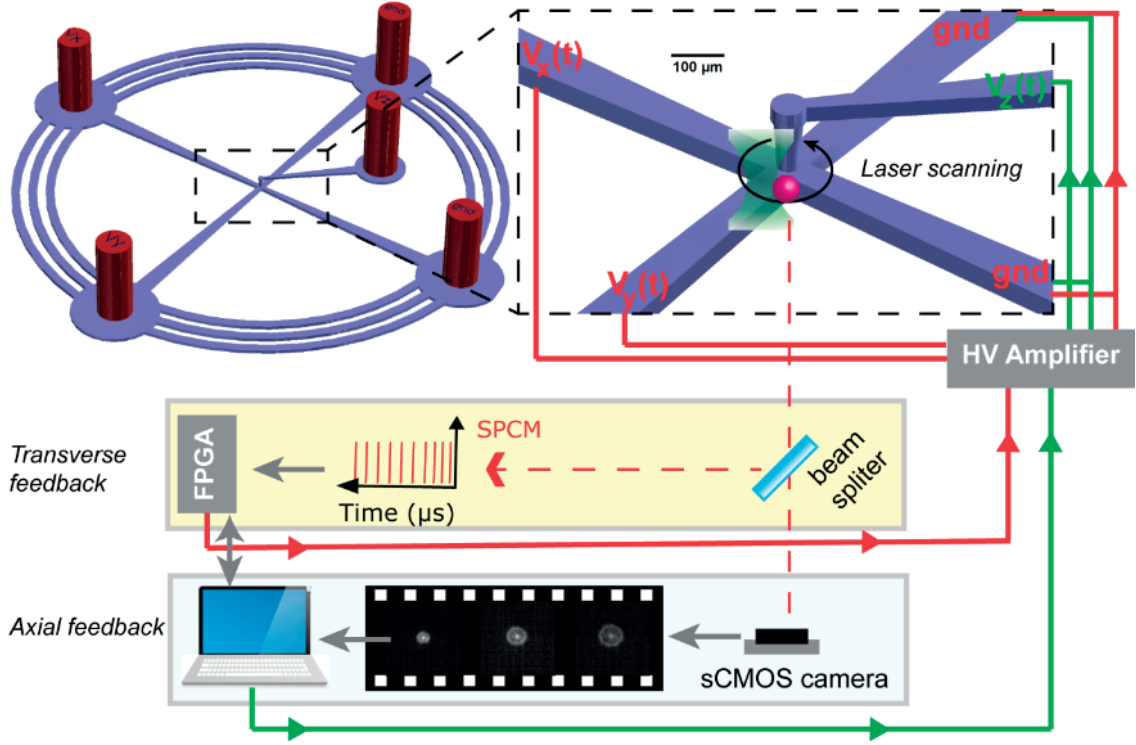
Figure 3.1: The schematics representing the microfluidics geometry. Several outer rings are connecting the ports to suppress the undesired drifts in the channels. The trap chamber in the center connected to three orthogonal channels each for one-dimensional control. The feedback voltages on the electrodes (vx, vy, vz) generate the electric field actuating electrophoresis and electroosmotic forces. The ports are also functioning as inlet and outlet.

3.4 Three-Dimensional Position Tracking

The axial position of the particle was estimated through defocused imaging proposed by *Speidel et al.* [151]. The idea is to detect the off-focus distance that is encoded into the intensity pattern in the image plane. It is shown that for a point-like particle, the size of the outermost ring of the pattern scales linearly with the axial position. Here, we demonstrated the relation for a wide defocusing range starting from ≈1 μm above the focus plane (**Figure 3.2**). Since the random walk of a particle takes a time-bin of $t = \delta^2/2D$, where D is the diffusion coefficient and δ is the displacement, this range also defines the maximum feedback latency tolerated in a stable trapping. The optimal target position is chosen such that it extends the path a particle can travel before it escapes. Once the position determined the feedback is applied to the corresponding fluidic channel, this compensates the Brownian motion induced offset.
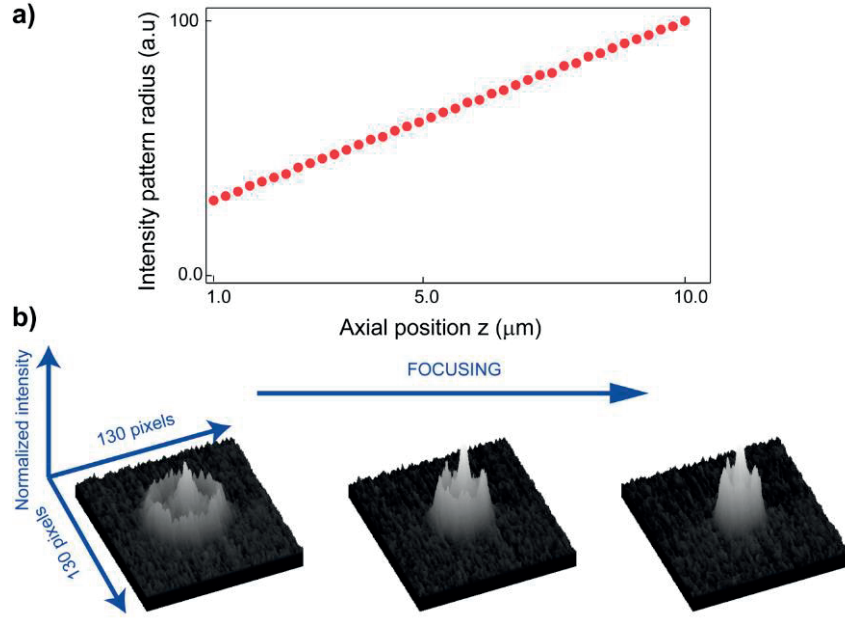
Figure 3.2: a) The size of the outermost ring in the intensity pattern of FND scales linearly with the distance to the focal plane, z. **b)** Surface profiles of the grayscale images visualizing the intensity patterns at three different axial locations. Defocusing stretches the pattern, enlarges the outermost ring size and degrades the image contrast.

While it has sub nanometer detection precision in the axial dimension, this detection scheme does not provide high spatial resolution in the transverse plane. A large defocus value leads to a spread in the intensity pattern and a consequential degrade in the image contrast where the location with the maximum intensity value defines the particle position in the transverse plane. Further, since the image processing for all dimensions extends the feedback latency, an independently running detection scheme is preferable for high temporal resolution. Therefore, the detection in the transverse plane was performed using a real time *Kalman filter* implemented on a field programmable gate array (FPGA) device and a rotating laser beam around the target point that excites the particle with a uniform profile as reported in *Kayci et al.* [61]. Using an avalanche photo diode (APD) that feeds the filter on the FPGA device, the positon vector can be precisely determined upon single photon arrivals. The correcting filter gain, adjusting the feedback strength, is determined by instant photon count rate and the geometry of the scanning beam (see **Supporting Information**). Similar to the axial trapping, to keep the particle at the target location, any shifts in the transverse plane is cancelled through the in-plane fluidic channels. While for the axial dimension the feedback rate is mainly limited by image processing speed (≈4 ms) and the camera exposure

time ($\approx$10 ms), for the transverse plane it is a function of photon counts on the APD and the frequency of the scanning laser beam.

3.5 Fluorescent Nanodiamond Trap

To test the performance of the presented three-dimensional ABEL trap, we have used single FND due to their non-blinking and non-bleaching properties. Due to its optic and spin properties, NV embedded in a single FND has received a remarkable interest in the last decade. It has been validated as nanoscale quantum sensor for physical parameters ranging from temperature [58], pressure [70], and ion concentrations [71] to external electric and magnetic fields. As the particle presents no bleaching or blinking behavior under ambient conditions, it is well matched to the ABEL trap manipulation approach. More recently, we showed such FNDs could be used as sensitive magnetometer in two-dimensional ABEL trap operating in fluidics [61]. After the successful realization of the hybrid detection scheme in the tracking, here we verified the performance of technique by three-dimensional trapping and scanning of 25 nm sized single FNDs.
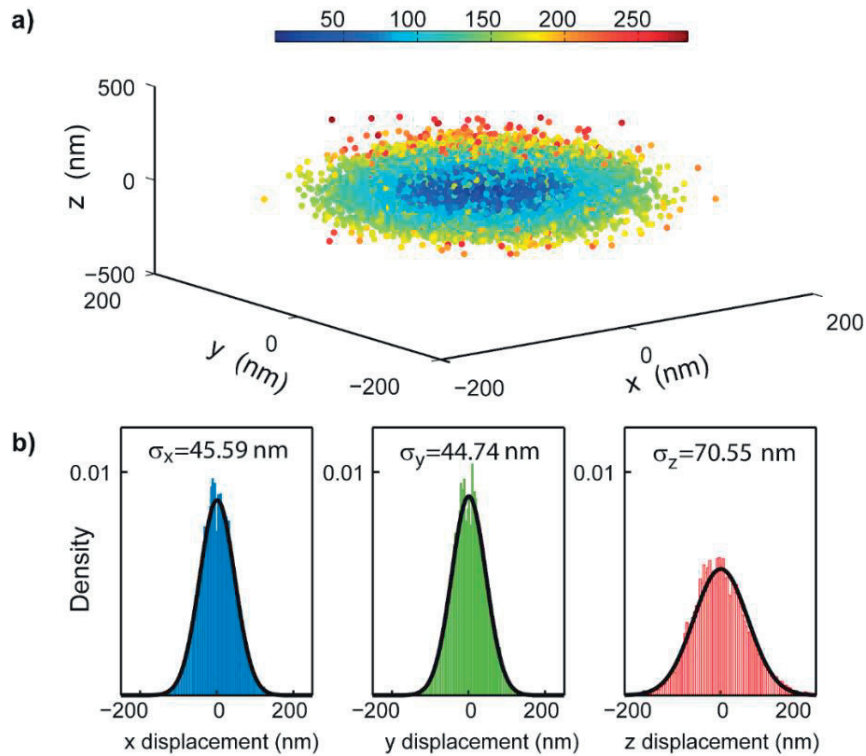

Figure 3.3: a) The estimated positions at which the FND was detected during a trap event. The color bar visualizes the distance to the target point **b)** x, y, z displacement histograms during the trap event. The confinement in the transverse plane (x, y) is better than the axial dimension due to the fast detection scheme.

The particle was confined to a nanoscale volume with the displacement values of $\sigma_x = 45.59$ nm, $\sigma_y = 44.74$ nm and $\sigma_y = 70.55$ nm and thereby setting the trap stiffness (**Figure 3.3**). As the uniform excitation is performed by a rotating pencil-like beam with a high depth of focus and the particle is not photo bleaching or blinking, the emission follows a digital profile when the trap sate switches (**Figure 3.4**). Three-dimensional scan of the relative position in the buffer was performed using a nanopositioning stage. Basically, the displacement of the stage was conceived as perturbation to be cancelled by the electrokinetic forces as done for the fluctuations driven by the Brownian motion.
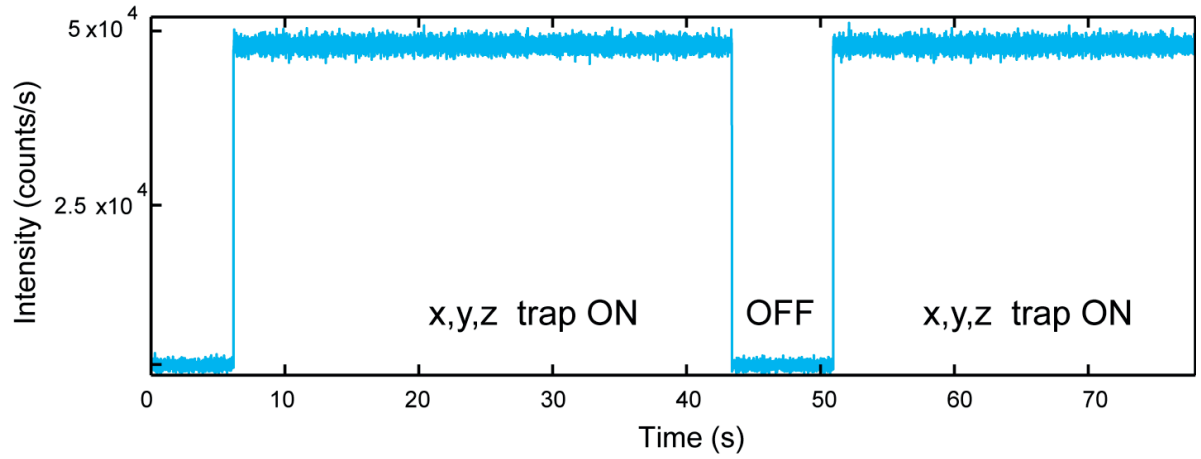
Figure 3.4: The photon counts on the APD when the trap state switches. The profile verifies non-photo bleaching and non-blinking behavior of the FND. The high contrast in the profile demonstrates the feasibility of sensing and detection applications exploiting fluorescence decay at magnetic resonance. The intensity of the trapped FND remains constant in the whole axial range corresponding to 10 um when FND is scanned with the nanopositioning stage. Current design of microfluidic chip limits the axial range to 10 um.

3.6 Conclusion

Combining computationally independent detection schemes, scanning laser beam guided position estimation, and defocused imaging, high frequency three-dimensional particle tracking is demonstrated. The method is verified by ABEL trapping of a single 25 nm sized FND containing NV defects diffusing in fluidics. The microfluidic cell is fabricated through the soft lithography process of PDMS. Extension of the ABEL trapping into the third dimension facilitates the scanning of the trapped particle in the fluidic volume where the temporal and the spatial scanning resolutions are

limited by the nanopositioning stage. This provides a remarkable sensing tool to map the three-dimensional distribution of the physical quantities in a fluidic environment.

3.7 Supporting Information

3.7.1 Image Processing Based Position Estimation for Axial Dimension

The images are acquired through a fast CMOS (Andor Neo) camera streaming the data into the computer. The region of interest is set to the maximum size that the intensity pattern of the target particle can reach during the active feedback intervals. Image processing is performed on NI Vision Module environment. A threshold suppressing the background noise is applied to the luminance data extracted from the image frames. This process also filters any particle with the intensity value falling outside of the threshold range, which provides selectivity. After subsequent *dilute*, *erode* operations with the calibrated parameters, the size of the outmost ring in the intensity pattern is detected through processed image in binary (**SI Figure 3.1**).
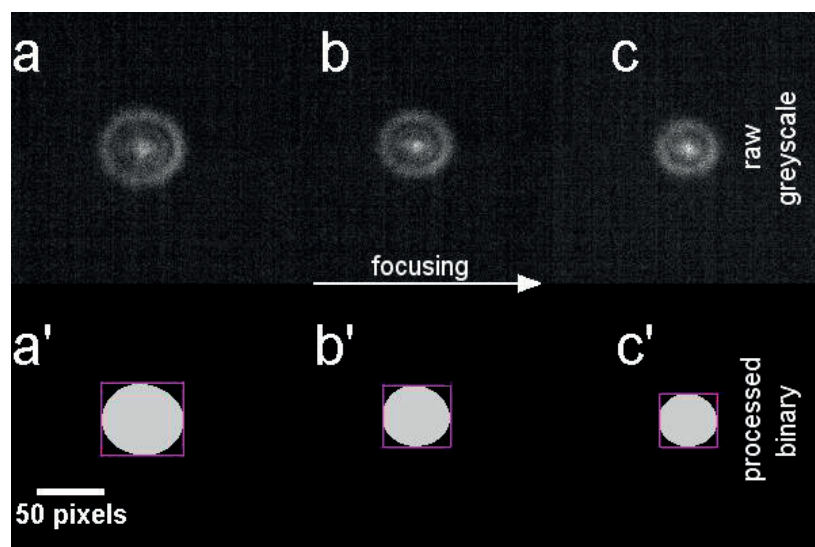
SI Figure 3.1: Selected image frames obtained using sCMOS camera. Simple and fast image analysis extracts the particle axial positions based on the estimation of the size of the outer most ring in the intensity pattern (a, b, c). The results of the image processing are displayed in (a', b', c') for the corresponding frames.

### 3.7.2 Kalman-Filter Based Position Estimation in the Transverse Plane

In this approach, a pattern is fed into electro optic deflectors scanning the sample plane. Then through fluorescence photons arrival times (detected by a Single Photon Counting Module SPCM), the position of the molecule is obtained. As the beam has a finite size, these positions are not precise and so-called measured positions with a measurement noise. A digital filter, Kalman-filter, is used to estimate the real positions. A summary of the recursive algorithm is given in section 1.3.3. The filter is implemented in a NI-FPGA device). Details on the set-up can be found in *Kayci et al*. [152].

3.7.3 Microfluidic Cell Fabrication

The SU8 master defining the geometry of the transverse plane microfluidics was fabricated in many layers that the thickness of the channels is minimum around the trap chamber. This facilitates better electrical contact for the electrodes and higher electrokinetic mobility in the trap chamber. The microfluidics were formed using PDMS spin coating of the master with a thickness value setting the depth of the trap chamber. Then, the mold was peeled off and transferred to a clean PDMS base for punching process (**SI Figure 3.2**). The location of the trap center was punched as circular cavity of 300 µm in size to connect the fluidic channel in a second layer. Similarly, the fluidic channel in the second layer was made and plasma bonded to the first layer such that the end port of the channel enclosed the trap chamber (**SI Figure 3.3**). This connection couples the control into the axial dimension. The alignment was performed precisely under a microscope. Then, the cell was punched to introduce the integration ports for electrodes. These ports also serve as inlet and outlet for the sample. Finally, the microfluidic device was plasma treated for hydrophilic property and assembled by the integration of a glass cover slip (**SI Figure 3.4**).

SI Figure 3.2: Photograph of the transverse plane microfluidics formed in a thin PDMS layer. The layer is transferred to a thicker one for punching process, which defines the trap chamber.
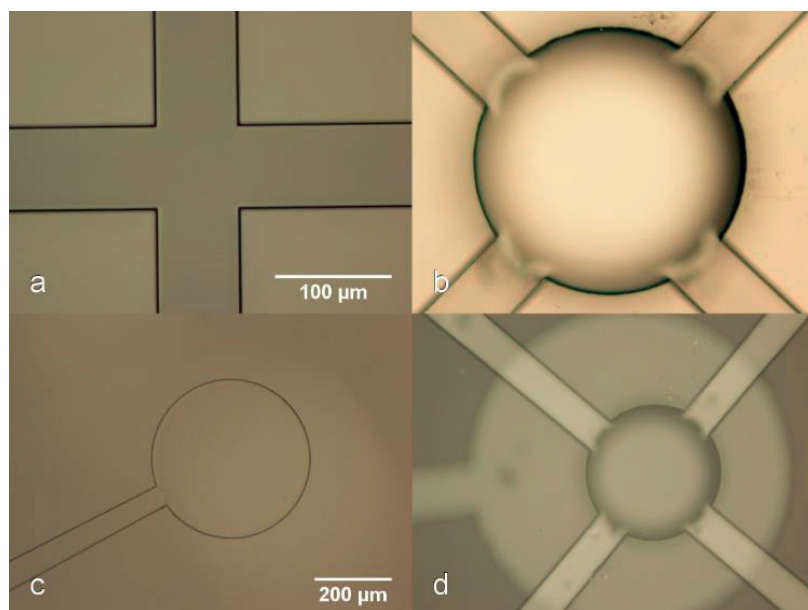
SI Figure 3.3: Bight-field optical micrographs of the layers of the microfluidics assembly. (a) The microfluidic channels formed in the first layer to be used in the transverse plane position control. (b) The trap chamber is formed at the intersection of the channels using a punch tool. (c) A single channel in a second layer is formed and used in the axial position control. (d) Two layers of the microfluidics are cascaded to introduce 3D position control for the particle diffusing in the trap chamber.
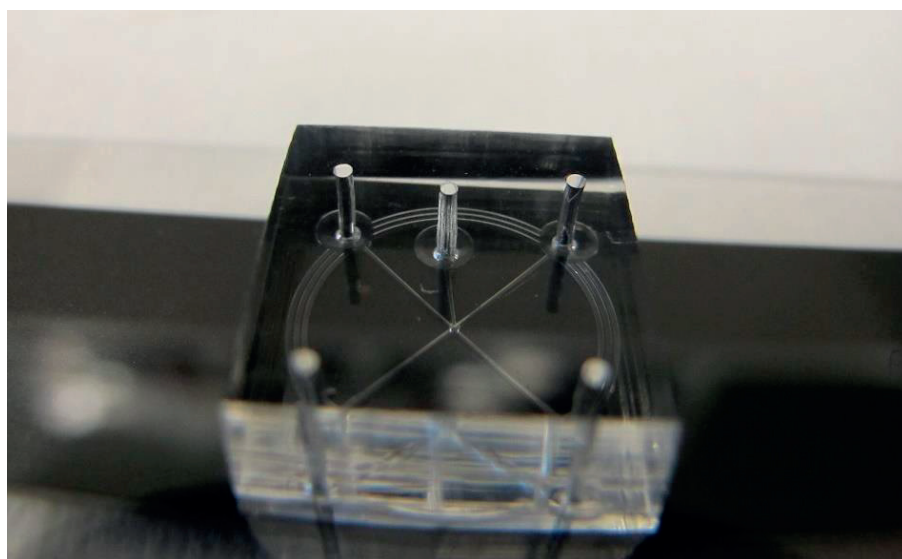
SI Figure 3.4: Photograph of the three-dimensional ABEL trap microfluidic chip. The ports are punched for the integration of the electrodes and loading the sample.

4. Electron Spin Resonance of Nitrogen-Vacancy Defects Embedded in Single Nanodiamonds in an ABEL Trap

4.1 Abstract

Room temperature optically detected magnetic resonance of a single quantum object with nanoscale position control is an outstanding challenge in many areas, particularly in the life sciences. We introduce a novel approach to control the nitrogen-vacancy (NV) centers hosted in a single FND for which an ABEL trap performs the position control and an integrated Radio Frequency (RF) circuit provides enhanced magnetic flux density for ensemble spin-state control simultaneously. We demonstrate static magnetic field sensing in platforms compatible with ABEL trap. With the advances in the synthesis and functionalization of stable arbitrarily small FNDs, we foresee the use of our device for the trapping and manipulation of single molecular-sized FNDs in aqueous solution.

4.2 Introduction

The progress in fluorescence imaging is determined by our ability to create bio-imaging probes that will not saturate blink, nor photobleach, should not be destructive nor toxic. Recently, novel probe in the form of FNDs has been introduced as an appealing alternative to fluorescent proteins and organic dyes. FNDs contain built in fluorophores, most often in the form of the defects, such as nitrogen vacancy complexes (e.g.NV^-) [153]. The NV defects are atom-like and form photoluminescent color centers which render them exceptionally photostable [154]. Besides bio-imaging applications, the NV defects in the FND lattice are promising candidates for quantum optics and nanoscale metrology. It is demonstrated that FND can be a stable single photon source [155] and an emitter system to provide optically accessible spin qubits [156]. Recently, electric and magnetic field sensing [56, 87, 88] thermal sensing [58, 94], and single photon microscopy [130] has been achieved using single NV defects. In addition, a NV based magnetic sensor works under

ambient conditions, and it is biocompatible, which makes it an excellent candidate for bio-imaging. So far, precise spatial control of single FNDs has been achieved using various modalities of scanning probe techniques [55, 87, 88, 130, 133]. However, this practice is less suitable in closed fluidic environments, such as the interiors of microfluidic channels. Laser tweezers present a compelling alternative to precise nanopositioning of nanostructures, owing to their ability to act in situ, in closed aqueous chambers and their potential applicability to a broad range of dielectric materials [109, 157]. Indeed, laser tweezers have been recently successfully employed to detect electron spin resonance (ESR) of nitrogen-vacancy centers in ensemble FNDs [135] and single FNDs [136]. Although as an attractive alternative to scanning probe techniques, detection of the ESR of nitrogen-vacancy centers in a single FNDs remains a challenge due to the inherent limitation of laser tweezers. The force employed by laser tweezers scales with the volume of the trapped object. For example, to trap a 10 nm object, this requires six orders of magnitude and as much input power to trap a 1μm object, which renders the trapping of the objects smaller than 100 nm challenging since it requires high laser powers (~150 mW) [136] and high fluid viscosity (5 cP) [137]. In addition, since the force arises through a second-order interaction of the trapped object with the applied electric or magnetic field, the field must first polarize the object, and then it can generate the force between the induced dipole and a gradient in the field. A further drawback of the optical trapping technique is its lack of selectivity. Optical trap generates a potential minimum for polarizable objects. Any sufficiently large polarizable object will be attracted and will fall into this minimum and be trapped. Laser tweezers cannot be used in dense dispersions because the trap will become overfilled by particles [158]. Moreover, high powers of the trapping laser might be too invasive for live cell magnetometery applications.

The ABEL trap is a novel non-perturbative technique [159, 160] that allows the trapping and manipulating of single fluorescent molecules in solution phase. It operates by tracking the Brownian motion of a single fluorescent particle in solution, and applies a time dependent electric field to induce an electrokinetic drift that cancels the Brownian motion. As the Brownian motion of different freely diffusing objects is uncorrelated, the applied potential cannot cancel out more than a single molecule Brownian motion at a time, which therefore provides required selectivity [161]. So far, ABEL trap has been used for the trapping of DNA oligomers [162, 163], photosynthetic protein allophycocyanin (APC) [164], G-Protein Coupled Receptors [165], and even single organic dyes [138, 166] with the photobleaching limited trapping period.

Here, we demonstrate an alternative scanning technique for magneto-optical spin detection under ambient and aqueous conditions by means of an ABEL trapping. Compared to the scanning

techniques using embedded NV defects in a functionalized probe tip [55, 87, 88, 130, 133], ABEL trapping does not require a physical support and provides a new window into the complex fluidic environments. By using the ABEL trap, we control the position of a single FND particle containing NV defect centers in solution phase. As the NV defect has non-bleaching behavior, the trap period is not limited by photobleaching and in consequence, trapped FNDs can be localized to a very high precision. The near fields of an integrated RF circuit, together with a green laser, enable us to excite the NV defects and change the spin-dependent luminescence intensity for electron spin resonance measurements.

4.3 Results and Discussion
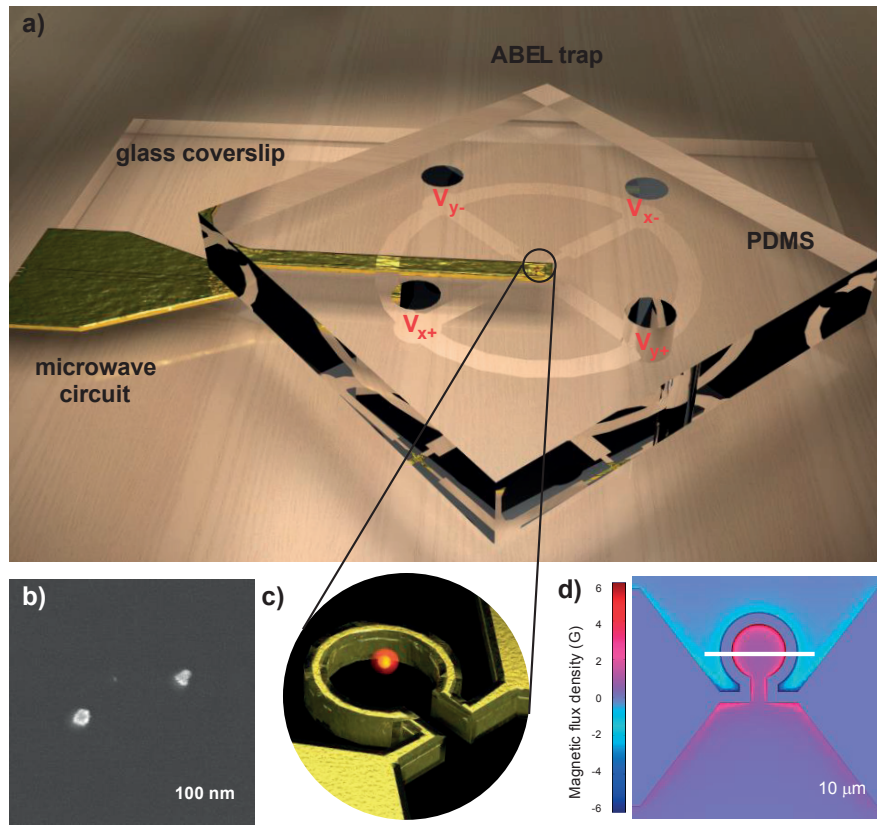
Figure 4.1: a) Schematic of ABEL trap PDMS microfluidic cell with RF circuit integrated on the same glass coverslip. **b)** SEM micrograph of 30 nm big fluorescent nanodiamonds. **c)** Zoom in the trapping area shown in **a)** indicating the relative location of FND in respect to the area with the enhanced homogeneous magnetic flux density. **d)** Finite element analysis of the magnetic flux density in the discontinuity area of the coplanar waveguide when excited with a power of 20 dBm at 2.87 GHz.

The ABEL trap performance significantly depends on the symmetry of the Polydimethylsiloxane (PDMS) chamber [167] and in our case, the trapping chamber had to be integrated with RF circuit, realized on the same cover-glass, as shown in the schematics **Figure 4.1 a)** and **c).** After finding the optimal PDMS trap geometry, (see *materials and methods*) we have performed finite element analysis with an aim to test several RF circuits that will deliver relatively homogenous magnetic flux density. As shown in the **Figure 4.1.d)** chosen RF circuit delivers homogenously magnetic field intensity of 2G in the discontinuity area of the coplanar waveguide when excited with a frequency of 2.87 GHz. Prior to trapping measurements, we have characterized sonnicated FNDs using Scanning Electron Microscope (SEM). Although, many FNDs are still in aggregated form (data not shown) it is possible to find without difficulty numerous isolated FNDs as shown in the **Figure 4.1. b)**. The ABEL trapping experiments were performed in a purpose-built optical set-up detailed in the **Figure 4.2 a),** similar to one reported in Ref [138, 160]. In our set-up for single molecule fluorescence detection, one can either use fast CMOS (Neo Andor) camera, having a feedback rate up to 400 Hz, or Avalanche Photodiode APD, having a feedback rate up to 97.34 kHz, for details see *materials and methods*. Before trapping, we investigated the optimal laser scanning radius as shown in **SI Figure 4.1.** To test the performance of our ABEL trap, we first trapped fluorescent 20-nm beads (fluospheres 'red-orange' 580/605, F8786, Molecular Probes). We succeed in a trapping of these 20-nm fluorescent polystyrene beads for up to 20 seconds **(see SI Figure 4.2.a)**. Unsurprisingly, intensity profile indicates slow photobleaching of multiple fluorophores contained in single 20-nm bead. In addition, the ABEL trap performance was validated by cross-correlating positions measured using CMOS camera and positions extracted from the voltage vectors applied by the feedback using APD **(SI Figure 4.2.b)**.
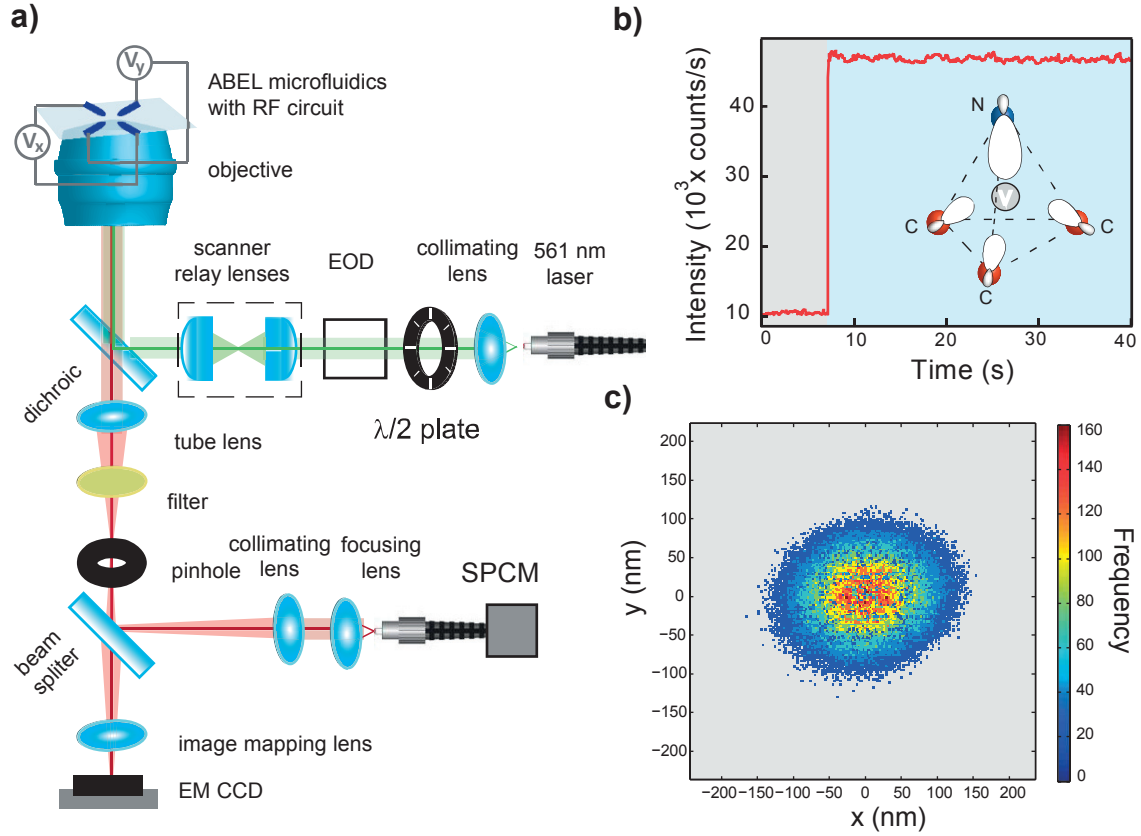
Figure 4.2: a) Schematic of ABEL trap optic set-up. The pair of electro optic deflectors (EODs) introduces an angle to the input beam with the voltage vector generated from the high voltage amplifier. The scanner relay lenses are coupling the angles to a position vector that forms the optic pattern in the sample plane. Confocal detection is performed with a pinhole placed in the 1st image plane. Beam splitter enables detection paths for camera and single photon counting module (SPCM). The filter implemented on the FPGA applies the feedback voltages to the high voltage amplifier based on the TLL pulse counts from the SPCM. **b)** Fluorescence intensity profile of trapped and not trapped single FND, when the feedback is on (blue area of the graph), a single FND entering the target region is trapped. As the particle does not show photo bleaching characteristics, it became trapped as long as the feedback is on. Inset shows lattice structure of the NV defect in FND**. c)** Position histogram of the trapped FND.

After successful realization of the ABEL trap, we proceeded with the trapping of 30-nm-sized single FNDs that contains approximately 10 NV defects (**Figure 4.2.b, c**). The ABEL trapping, as for the 20 nm fluorescent beads, has been achieved through transversal electrokinetic forces generated in the microfluidics while the out-of-plane movements are physically restricted by the trap cavity walls. The position deviation introduced by thermally driven Brownian motion is suppressed with the closed-loop feedback control system. High diffusion coefficient of the single FND requires a very fast position-sensing scheme and feedback update that are not possible with camera-based solutions. Although, as in the case of optical trapping, we could increase viscosity [136] to allow camera-based detection for the trapping of single FNDs, having APD with the feedback rate up to 97.34 kHz was

not necessary. The position in the transverse plane is estimated via a Kalman-filter implemented on a field-programmable gate array (FPGA) with a scanning Gaussian beam and confocal fluorescence signal detection on a single photon counting module (see *materials and methods*). The feedback voltages generating the electrokinetic forces are applied to orthogonal pairs of platinum electrodes integrated to the trap cell.

In the absence of the feedback, the 30 nm sized FNDs diffuse across the excitation pattern so fast that the contribution to the total fluorescence can be detected only by a detection system with the sub millisecond temporal resolution. Thus, photons are counted through an avalanche photodiode (SPCM-AQRH-14, Perkin Elmer) that generates a transistor-transistor logic (TLL) pulse train with 350 ps timing resolution. When the feedback was applied, only one of the diffusing FNDs was tracked and trapped to a sub-micron area **(Figure 4.2.c)**.

Feedback rate of 20 kHz [138, 160] is sufficient to stably trap single 30 nm large FND for tens of minutes. In contrast to the intensity profile of single 20 nm fluorescent polystyrene beads, we observe no photobleaching **(Figure 4.2.b).** Our observation is in accordance with previous results on the characterization of surface bound FNDs [168]. Electronic spin states of the NV defects in single FNDs were excited with the same laser, λ=561 nm, used for tracking. FND displacement distribution is shown in the form of a 2D histogram **(Figure 4.2.c)**. Full with at half maximum values for x and y dimensions, $fwhm_x = 130$ nm and $fwhm_y = 120$ nm have set our localization precisions for single FND. Finally, we have shown that trapped single FNDs can be scanned over the trap area using nanopositioning stage that is an integral part of our set-up.
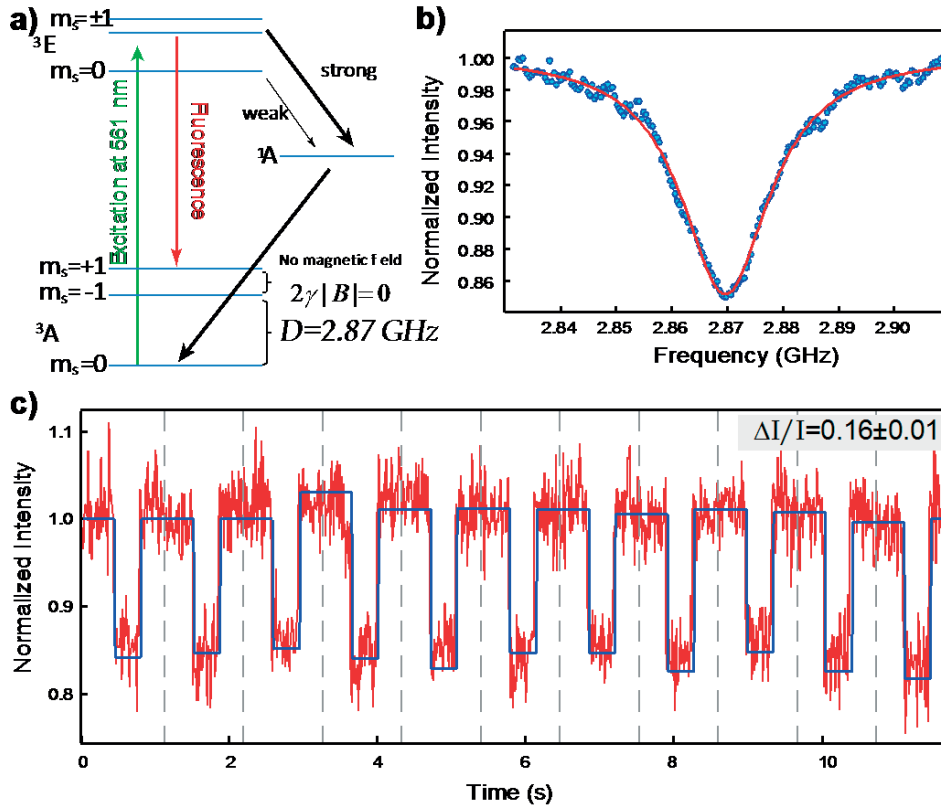
Figure 4.3: a) The energy diagram of the ground state 3^A, excited state 3^E and metastable singlet state 1^A represented for NV. Dashed black arrows show the non-radiative decay via the singlet state. **b)** ODMR spectra of NV defects in trapped FND. Microwave frequency swept in 1 MHz intervals of 10 ms dwell time. **c)** Observation of the electron spin resonance at 2.87 GHz with 1:2 on:off microwave excitation. The dwell time was set to 200 ms.

Having in-hand a method for manipulating, positioning, and characterizing single FNDs, we set out to perform ensemble spin state control of the NV defects. This has been realized via a RF circuit patterned on a thin coverslip integrated to the ABEL trap microfluidics **(Figure 4.1.a)** (See *materials and methods*). The engineered geometry of the discontinuity on the coplanar waveguide transmission line couples uniform oscillating magnetic fields to the NV defects over 100 um area that can be used for scanning purposes in the ABEL trap as well as other bio-experiments for bulk measurements. To probe the frequency dependent coupling to the defects, a parametric sweep measurement with 1 MHz modulation and 10 ms dwell time was performed. The spin-dependent PL intensity of the NV defects has been collected with the same APD used for the position detection in the ABEL trap. The photoluminescence drop around the resonance frequency showed a *Lorentzian* line shape, similar to the ones reported for the bulk measurements **(Figure 4.3.b)**. In addition, pulsed RF signal at the resonance frequency was applied with the extended dwell time,

200 ms **(Figure 4.3.c).** Our results demonstrate that the observation window at resonance could be extended to allow better estimation of the changes in the spin-dependent PL intensity.

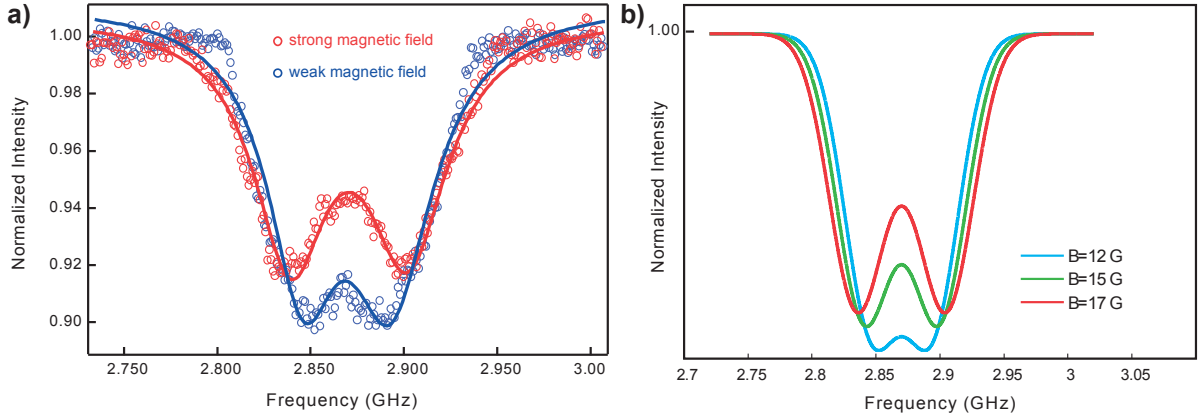**Figure 4.4: a)** Optically detected ESR spectra of an ABEL trapped single FND under presence of the weak and strong static magnetic field. The solid lines represent two-Lorentzian fit defining transition frequencies. For the strong magnetic field, we find f_{01}= 2838.7 ± 0.385 MHz and f_{02} =2901.7 ± 0.411 MHz. While for the weak magnetic field we obtained f_{01}=2844.7 ± 0.665 MHz and f_{02} =2892 ± 0.736 MHz. The data points in the frequency sweep were acquired in steps of 1 MHz. **b)** Modeled ESR spectra of rotationally diffusing single FND in the ABEL trap at several magnetics field strengths. It is assumed the orientation of the particle acquires a random phase on each feedback step. By comparing the measured frequencies with our model, we can extract the values for the strong and weak magnetic fields (~16 G and ~14 G).

The NV centers in the ABEL trap are not fixed in orientation. Therefore, we modelled the ESR spectra of the particle exposed to the random rotational motion (See *supporting information)*. Basically, the 'random walk' of the angle between the NV symmetry axis and the microscope objective, that is fixed with respect to the external magnetic field, leads to a change in the NV excitation level, the emitted fluorescence collection efficiency and the strength of magnetic field component aligned with the spin orientation. The contributions of uncorrelated angles form the spectra with two broadened peaks split by a frequency that is dependent on the applied magnetic field strength. A similar profile has been shown by *Horowitz et al.* [135] for the optic trap of NV defects oriented with isotropic density. To examine rotationally free characteristic of the particle in the ABEL trap, we performed ESR experiments in the presence of static magnetic fields. Obtained measurements are consistent with the model **(Figure 4.4)** and demonstrate the possibility of sensing static magnetic fields in platforms where the ABEL trap is compatible. Moreover, a recent work by Maclaurin *et al* [139] on a free diffusing diamond nanocrystal as sensitive magnetometer for fluctuating and

oscillating fields validates the ABEL trap approach for magnetic sensing in a closed fluidic environment.

4.4 Materials and Methods

4.4.1 Fluorescent Nanodiamond (FND)

30 nm big FNDs were produced by helium-ion irradiation and thermal annealing of type Ib diamond nanocrystallites, followed by oxygen etching in air and surface functionalization [63]. FNDs were thoroughly washed and re-suspended in water at 1mg/mL concentration with single FND having approximately 10 NV centers. To minimize FNDs precipitation and agglomeration, we sonicated the sample prior to each ABEL trapping experiment.

4.4.2 The RF Circuit

The total Hamiltonian of the NV defect is given by [169-171],

$$H = D(s_z^2 - S(S+1)/3) + E(s_x^2 - s_y^2) + \gamma \vec{B}.\vec{S} + H_{SI} + H_I$$

where D and E are zero-field splitting (ZFS) parameters, γ is spin gyromagnetic factor, $\vec{B}$ is vector magnetic field, H_{SI} is hyperfine coupling to the ^{14}N nucleus (spin I), and H_I is the nuclear term. Neglecting the nuclear interaction and external magnetic field, only the ZFS term will be focused. Owing to its C_{3v} symmetry [69], the transverse parameter $E = 0$ and the sublevels $\langle m_s = 0 \rangle$, $\langle m_s = \pm 1 \rangle$ are separated by the energy equivalent to the parameter, D =2.87 GHz **(Figure 4.3.a).** In this case, a microwave source at the resonance frequency $f = D$ will excite the optically populated $\langle m_s = 0 \rangle$ states to the $\langle m_s = \pm 1 \rangle$ states. As the NV centers in $\langle m_s = \pm 1 \rangle$ states have higher probability of undergoing intersystem crossing [172] (ISC), this control mechanism serves as the basis for optically detected magnetic resonance (ODMR).

In our set-up, the green laser, λ=561 nm, used in the ABEL trap for tracking, also operates as the optical pump for $\langle m_s = 0 \rangle$ states. The microwave excitation of these states has been realized using the enhanced magnetic field generated near the discontinuity on a coplanar waveguide transmission line (**Figure 4.1.d**). This configuration was used for two reasons. First, all the conducting material is on the same surface of the dielectric that avoids the optic blockage. Second, the geometry does not require presence of via holes that are difficult to realize on a thin cover glass. The enhancement of the field is due to the evanescent or non-propagating higher modes defined by the modified boundary conditions of the waveguide. The design of the CWG transmission line

was accomplished by using TXline and 3D finite element analysis of the electromagnetic characteristics of the discontinuity carried out via COMSOL 4.2 RF Module.

4.4.3 Kalman-Filter

The filter **(Table 4.1)** implemented for the ABEL trap experiments is derived from the original algorithm [173] and is the one used in the Cohen group [138]. The recursive nature of the filter enables a real time process using only present measurements and previously estimated parameters; full history of estimation is not required. The filter minimizes the mean of the squared error in the position estimation through predict and update steps.

Update $\left[\gamma = p_{k,k-1}(p_{k,k-1} + 2w_0/n)^{-1}\right]$ **Predict**

$r_{k,k} = r_{k,k-1} + \gamma(EOD_{x,y} - r_{k,k-1})$	$r_{k,k-1} = r_{k-1,k-1} + \mu dt u_{k-1}$
$p_{k,k} = p_{k,k-1}(1 - \gamma)$	$p_{k,k-1} = p_{k-1,k-1} + 2Ddt$

Table 4.1: The Kalman-filter parameters used in the ABEL trap experiments.

Basically, there are two parameters propagating, $r_{b,a}$ and $p_{b,a}$, which are the mean and variance estimates for position of the particle at time b given all the data up to and including time a, respectively. The Kalman gain, γ, is the correcting factor for update step and scales the contributions of the measurements and the current state. $EOD_{x,y}$ is the position of the rotating beam in the sample plane with beam size, $2w_0$ (**SI Figure 4.1**). u is the feedback voltage vector where dt is the time period between the two consecutive update steps and μ, D are the electrokinetic mobility and the diffusion constant of the particle, respectively. γ is modelled such that it converges to unity when we have a very small beam waist size, w_0, leading to the higher resolution in scanning, and very large photon counts, n, which implies that the probability of hitting the molecule with the laser beam is at maximum. In this case, the update is determined by the laser position, $r_{k,k} = EOD_{x,y}$. While for the counter case (γ converges to zero), we do not trust the laser position and we use the previous estimates, $r_{k,k} = r_{k,k-1}$ and $p_{k,k} = p_{k,k-1}$.

4.4.4 Scanning Pattern

The scanning pattern is generated through a rotating pencil-like Gaussian beam that is perpendicular to the sample plane. The beam waist $w_0 \approx \lambda/\pi NA$ um and $\pi\ 2\pi w_0^2/\lambda \approx 7$ um were set via the focal length ratio of the scanner relay lenses (**Figure 4.2.a**) controlling the radius of the collimated beam, w, entering the objective where $NA \approx w/f_0$ is the numerical aperture, $\lambda = 561$ nm is the operating wavelength, and $f_0 = 3.33$ mm is the focal length of the objective (Nikon 60X PlanApo $NA = 1.2$). For optimal tracking, the rotating beam should cover the trap area and ensure that the molecule will be excited even if it is in the trap center. The radius of the trap area, R_0, is the parameter to control the intensity distribution of the rotating beam on the scanning plane (see **SI Figure 4.1**). The intensity value of a point located at (x, y) is: $I(x, y, t) = I_0 e^{-\frac{2\left((x-x')^2 + (y-y')^2\right)}{w_0^2}}$, where $(x', y') = R_0(\sin \Omega t, \cos \Omega t)$, is the instantaneous position of the Gaussian beam center at time t. The average value over one cycle is

$I(x, y) = \frac{1}{2\pi}\int_{-\pi}^{\pi} I(x, y, t)\, dt = (4I_0 R_0 r/w_0^2)e^{-2(r^2 + R^2)/w_0^2}$, where I_0 is the 0th order of modified Bessel function, and r is the distance of the (x, y) point from the origin. The simulations (**SI Figure 4.1**) showed that the optimal scanning radius is $R_0 = 0.7w_0$ since it provides both a uniform and large excitation area.

4.4.5 RF Circuit Integrated Microfluidic Cell Fabrication

Microfluidic channels in PDMS were molded on SU8 masters in multi-layer form. A microfluidic depth of 800 nm in the trap center increases to 50 um towards the electrodes for electrical contact, confinement of the fields in the trap center and suppress of resistive losses. Several outer rings were used to suppress the bias pressure (See *supporting information*). RF circuit on cover glass was formed through 200 nm of Cr and 800 nm of Al evaporation. After the electrical isolation with 30 nm of Al_2O_3, the circuit was embedded in a PDMS layer of 4 um thickness to provide a flat surface for the microfluidics integration. The SMA connected chip then plasma bonded to the microfluidic cell with precise alignment under the microscope (See *supporting information*).

4.5 Conclusion

To summarize, here we demonstrated the position control and trapping of the single FNDs using an ABEL trap that employs electrokinetic forces generated through the real-time particle tracking and its position estimation. Trapped single FND (30 nm in size) was optically excited with the same laser,

λ=561 nm, used for the particle tracking. Microwave excitation of the spin states was performed using a RF circuit integrated to the trap platform. ESR spectrum upon the microwave excitation was detected and it is in agreement with the previous observation on fixed or optically trapped FNDs. In addition, we demonstrated that although the ABEL trapped FNDs are subjected to the rotations, our device is sensitive enough to detect the presence of the static magnetic field. Given the fact that the ABEL trap can already manipulate a single rhodamine molecule, with the progress in synthesis of the stable extremely small sized FNDs, we expect that our platform, in combination with the unique FND properties, opens up the possibility of performing a nanoscale magnetometry in closed fluidics environments.

4.6 Supporting Information

4.6.1 Inspection of Laser Guided Position Estimates
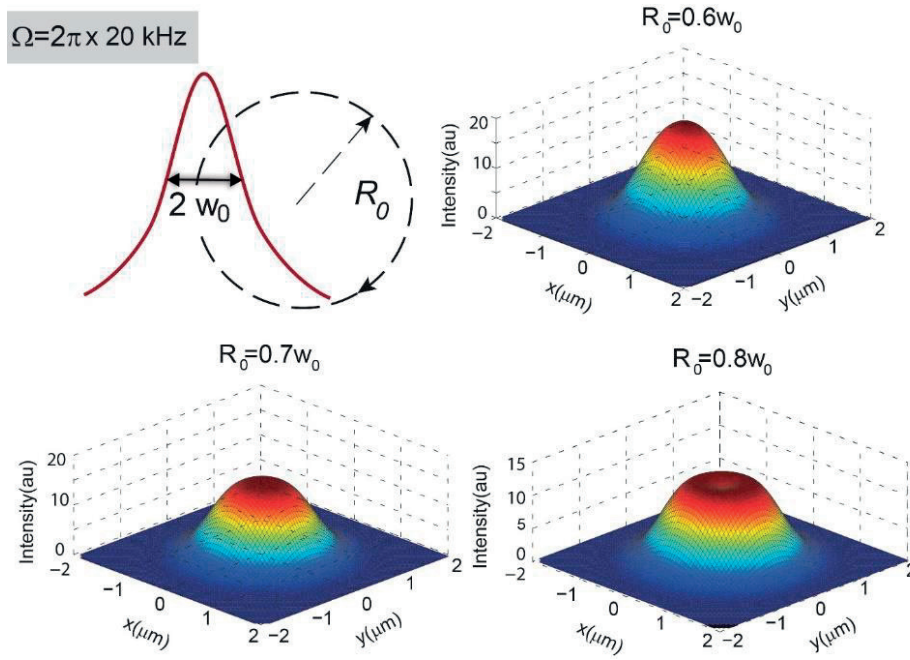
SI Figure 4.1: ABEL trap scanning configuration. Illumination profile of the rotating beam based on the varying scanning radius.

As the position estimates, based on laser scanning, is too fast compared to the camera frame, rates operation frequency of the FPGA was decreased to 4 kHz and the frame rate was increased to 400 Hz in a trap experiment with 20 nm sized fluorescent beads. The sampled voltages and frames were post processed to find an estimate for cross correlation coefficient. Position tracking of the bead in the frames was performed using NI LabVIEW. Despite the decreased operating frequency, photobleaching behavior of the bead (**SI Figure 4.2.a**), which degrades estimates on the FPGA and the synchronization error between the two channels, cross-correlation coefficient of 0.814, demonstrated that the laser guided particle tracking in the ABEL trap is quite powerful (**SI Figure 4.2.b**).
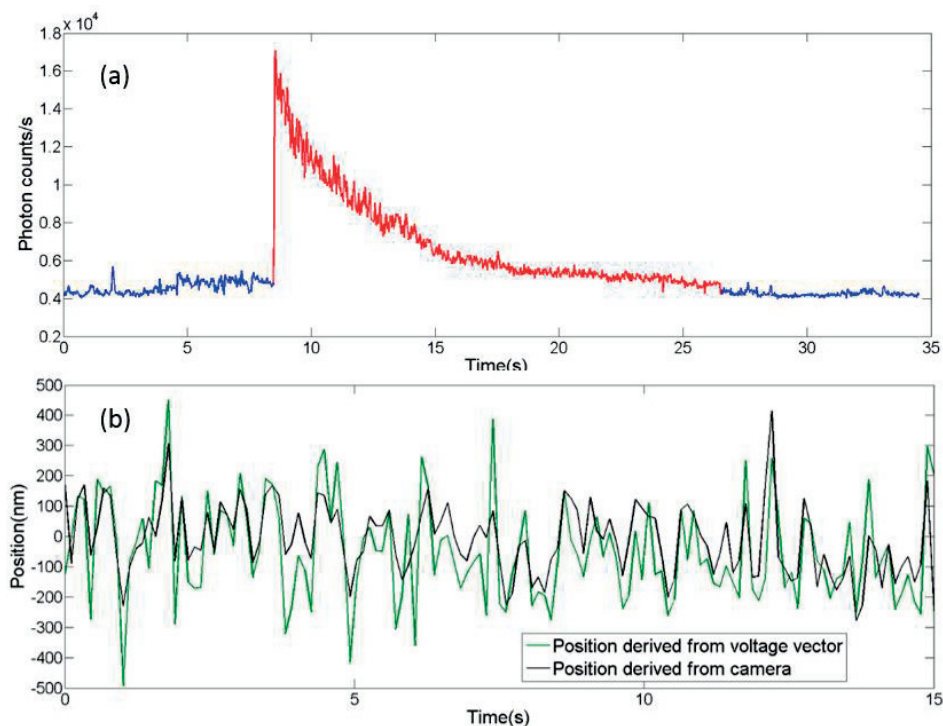
SI Figure 4.2: a) Photobeaching behavior of the trapped 20 nm sized fluorescent bead limiting the trap period. **b)** Position estimates of the trapped bead based on camera and the voltage vector on the FPGA.

4.6.2 PDMS on SU8 Master

For PDMS mold silicone base and curing agent at a weight ratio of 10/1 were used. After the degassing and curing process at 80° C, the mold was peeled off and 690 um sized holes were punched through the PDMS cell for the integration of the platinum electrodes and buffer loading. Several types of SU8 were used to fabricate the master in a 3-layers structure that forms the channels with non-uniform depth.
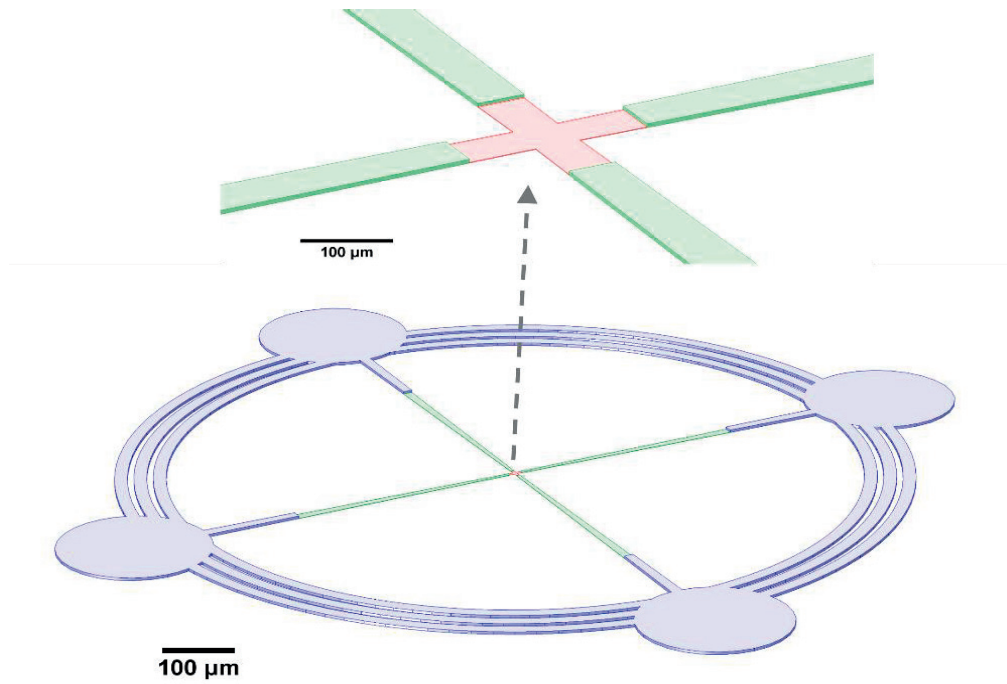
SI Figure 4.3: Layout of the SU8 master for ABEL trap microfluidics. The distance between the opposite ports for electrodes is 1 cm and the trap center has a size of 50x50 um.

Double side polished Si wafers 100 mm in size were plasma cleaned in Tepla300 for 20 minutes. GM1040 type SU8 was coated on the wafer with the following speed steps for 800 nm channel thickness: 5s at 500 rpm/s, 40s at 5500 rpm/s, 1s at 6500 rpm/s, 5s at 5500 rpm/s with 100 rpm/s ramp for all steps. After 1 minute of relaxation, the wafer was baked at 130 ^{0}C for 1 hour with 1 ^{0}C/min ramp. Then, 50 mW/cm^2 of exposure was done with MA6 trough backside alignment. A post-exposure bake at 90 ^{0}C for 15 minutes was performed for cross-linking before the second layer coating. GM1060 type SU8 was used to form 4 um thick of the second layer with the following spin steps: 5s at 500 rpm/s, 40s at 5000 rpm/s, 1s at 6000 rpm/s, 5s at 5000 rpm/s. The preceding process was similar to the first step with the following changed parameters: 10 minutes of relaxation time, 2 hours of soft bake, 95 mW/cm^2 of exposure, and 30 minutes of post-exposure bake. For a 50 um thick third layer, GM1075 was used with the spin steps as follows: 5s at 500 rpm/s, 40s at 3800 rpm/s, 1s at 4800 rpm/s, 5s at 3800 rpm/s. The process was completed with the following changed parameters: 10 minutes of relaxation time, 3 hours of soft bake, 120 mW/cm^2 of exposure, and 1 hour of post-exposure bake. The master fabrication (**SI Figure 4.3**) was completed with the

simultaneous development of the layers in p*ropylene glycol monomethyl ether acetate for 4 minutes and a hard bake at 150* ^{0}C for 3 hours.

4.6.3 RF Circuit on Cover Glass

The dielectric constant of the cover glass measured with the capacitance value obtained through thin metal evaporation on parallel surfaces of the material. The schematic of the circuit modelled on TXline and COMSOL RF Module.

Piranha cleaned 120 um thick cover glasses 24x60 mm in size were attached to Si wafers using quickstick135 for a double layer lift-off process. 200 nm of Cr and 800 nm of Al evaporated with LAB600H to pattern the RF circuit. After the sonication step in the acetone bath, the cover glasses were rinsed with isopropanol and DI water. 30 nm of Al_2O_3 was deposited on the circuit with ALD for the electrical isolation. The isolated circuit was embedded in a PDMS layer of 4 um thickness to provide a flat surface for the circuit and microfluidics integration. Using epoxy silver conductor (Ted Pella), the SMA end launch connector (Digi-Key) was aligned and attached to the circuit under the microscope. Finally, the circuit on the cover glass aligned with the trap center was formed in the microfluidic cell under the microscope and bonded through the plasma treatment (**SI Figure 4.4**).
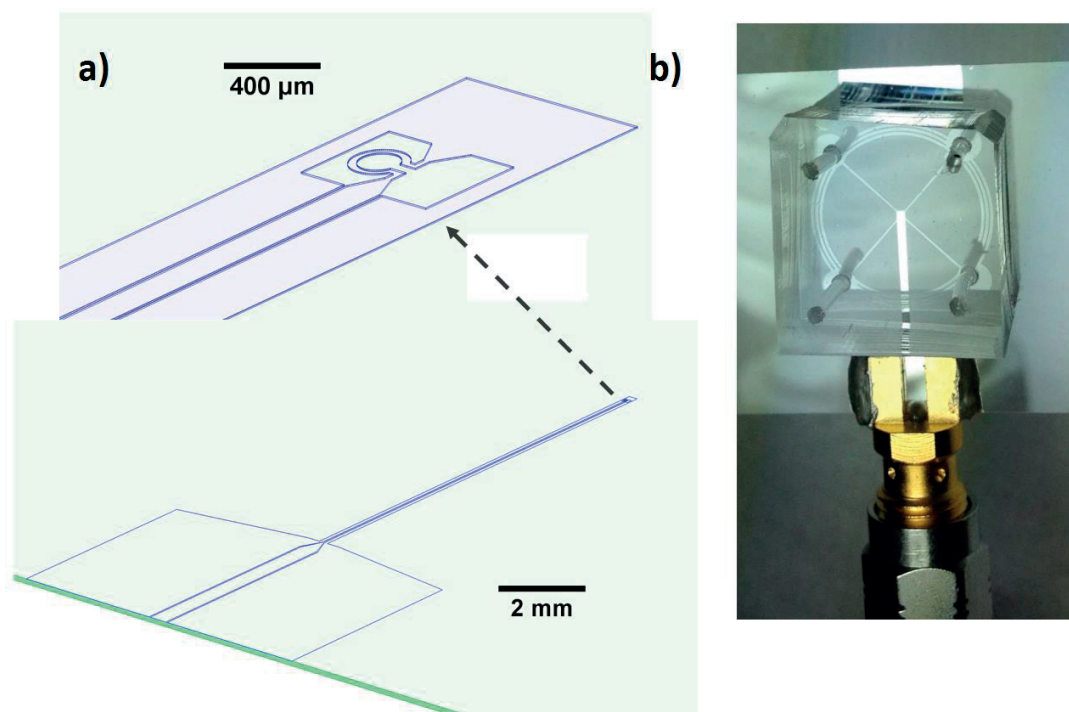
SI Figure 4.4: a) Modelled RF circuit schematic to be integrated to the PDMS cell. **b)** Photograph of the RF circuit integrated microfluidic device used for ESR measurements in the ABEL trap.

4.6.4 ESR Spectrum of a Rotationally Diffusing FND with NV Defects

The total absorption from optical dipoles, $\vec{p_1}$ and $\vec{p_2}$, that are orthogonally oriented [174, 175], with respect to the NV symmetry, is $A \propto |pE|^2$, where $p = \vec{p_1} + \vec{p_2}$ and E is the exciting electric field. The collection efficiency, C_{eff}, is limited by the critical angle of the microscope objective, $\alpha_c = \sin^{-1}(NA/n_w)$, where NA is the numerical aperture and n_w is the refractive index of water. $C_{eff} = \int_0^{\alpha_c} \int_0^{2\pi} I \sin\theta d\phi d\theta$, where I stands for the intensity of the dipole components orthogonal to direction specified by ϕ and θ spherical angles. For the NV at a specific orientation (ϕ, θ), with respect to the magnetic field, the influence on the ground state Hamiltonian is $H = D(s_z^2 - S(S+1)/3) + \gamma(B_z \cos\theta' + B_x \sin\theta' \cos\phi' + B_y \sin\theta' \sin\phi')s_z$, where B_x, B_y, B_z are magnetic field components and other parameters are as explained in the main text. To estimate the photoluminescence spectrum of a rotationally diffusing FND in the ABEL trap, we integrated 10^6 intensity profiles of the particle with random orientations. Increasing the magnetic field strength results in a separation in the frequency peaks with broadening and a decrease in the amplitudes **(Figure 4.4.b).**

5. Conclusion and Outlook

In the scope of this PhD work, I tried to establish a connection between electrokinetic manipulation and the diamond photonics. The ABEL trap technique has been selected as the manipulation tool for several reasons.

First, single FNDs with NV defects are bright and stable particles that are not photo-bleaching. While this property is not helpful for passive trapping techniques, such as optical tweezers, it fits very well to the tracking scheme followed in the ABEL trap. In this case, the trap stiffness and the size of the smallest particle that can be trapped are limited by the estimations and the active feedback performed in the digital environment. Therefore, future advancements in the FPGA device technology will enhance these parameters. An innovative solution for the speed enhancement would be a design in an application-specific integrated circuit (ASIC) platform.

Second, the ABEL trap uses weak electrokinetic forces that are not resulting in excessive heating and agglomerations. Moreover, the forces are not perturbative to the environment; all the molecules floating in the buffer are subjected to the same feedback. These properties are well matched to the quantum optic experiments carried on single FNDs.

Also, given that any physical support is not required, this technique is an outstanding alternative to AFM-like probes that are not functional in closed fluidic environments. The three-dimensional ABEL trap we proposed is able to manipulate single FNDs freely by diffusing in a fluidic volume. A potential future work could be a laser guided tracking scheme also employed for the axial position detection. One can perform time-shared excitations or multiple confocal detections on axial planes to extract the particle position with better temporal and spatial resolution [176, 177].

One drawback of the current ABEL trap configuration is the requirement of the cleanroom process for microfluidics. One potential solution would be glass nanocapillaries formed through a pipette puller. More recently, our preliminary work demonstrated that such nanocapillaries can be used for one-dimensional ABEL trap without any cleanroom process. A water-filled nonocapillary baked in liquid PDMS generates bubbles on its two ends that can be used for direct integration of electrodes. Besides its simplicity, nanocapillary configuration provides several advantages over the manipulation in PDMS microfluidics. In contrast to the PDMS, glass material has a very low background fluorescence noise. Furthermore, it does not adsorb molecules that may change the

surface quality. Given that glass is nonporous to oxygen, it will also reduce the quenching effect and extend the trapping period.

A far-out idea for the ABEL trap engineering would be the realization of a compact chip scale device that includes all the components required for a stable trapping. For instance, a micro electromechanical mirror (MEMS technology) can provide the same functionality as the scanning excitation optics, as shown in chapter 1. Similarly, a micro optical system for fluorescence detection may replace the detection optics. Although the miniaturization process requires a long term effort, once established it will be a very popular and practical tool for single particle studies.

After the realization of the ABEL trap, we have demonstrated the nanoscale magnetometry application of single FNDs in aqueous environment. This achievement also verifies the compatibility of the technique for other sensing and imaging applications single FNDs can provide. Besides the established detection protocols given in chapter 2, a potential future work would be the manipulation of functionalized aptamers coupled to single FNDs. If one end of a specific aptamer is attached to a magnetic bead and the other end is attached to single FNDs, the strong magnetic field will be reflected into the ODMR spectrum. As the proteins or lipids, specific to the aptamer, can break this connection manipulation of such complexes, the ABEL trap can present bio-sensing capability at the single molecule level. Compared to fluorescence resonance energy transfer (FRET) experiments, this approach has several advantages. First, as we are using magnetic labelling, the efficiency is not dependent on the donor-acceptor spectrum overlap. While in FRET experiments the distance between the donor and the acceptor should be in nanometer scale, for the proposed aptamer approach the ODMR signal only depends on the field generated from the magnetic particle, see **Figure 5.1**. Moreover, unlike FRET experiments, here the alignment of molecular orientation is not necessarily required. As the ABEL trap leads to an isotropic distribution in the particle orientation in time, the corresponding magnetic field strength can be precisely resolved. Given that enzyme-linked immunosorbent assay (ELIZA) technology is not providing required sensitivity for rare antigens, such a modality can open up new paths in clinical detection. However, we still need to investigate the temporal and spatial sensitivity of here proposed method to be able to fairly compare two modalities.
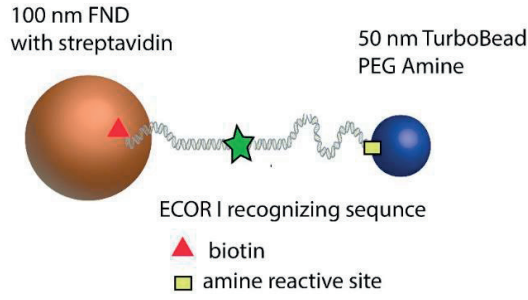
Figure 5.1: The aptamer configuration of single FND and magnetic bead for molecular specific detection. A bio-molecule that is modifying the aptamer will be visible in the ODMR spectrum.

The use of FNDs in aptamer configuration can also be employed in other single molecule techniques. For instance, NV centers, as magnetic reporter, in force-induced remnant magnetization spectroscopy (FIRMS) [178-180] can resolve noncovalent bonds between ligand-receptor complexes. This may facilitate studies on different systems of different complexities, such as protein-protein, protein-DNA, and DNA –DNA interactions. One possible configuration for the integrated platform is presented in **Figure 5.2.**
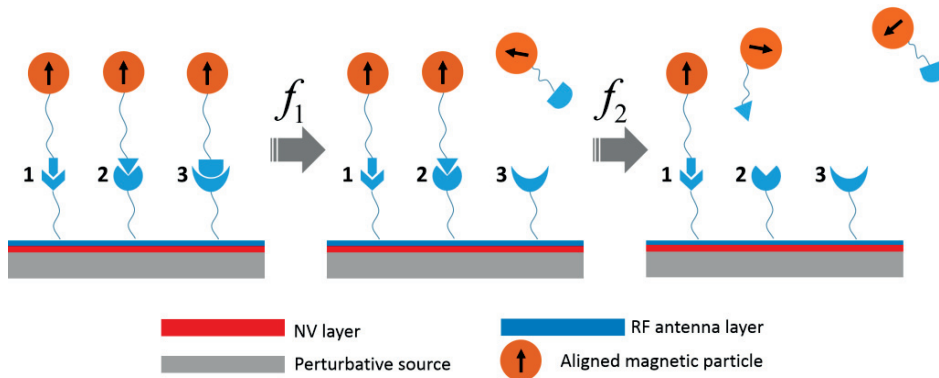
Figure 5.2: The working principle of NV magnetometry based force-induced remnant magnetization spectroscopy platform. 1, 2, 3 are standing for different ligand-receptor complexes. Different noncovalent bonds between the complexes are broken at different perturbative force strengths, $f_2 > f_1$. The dissociation process is randomizing the orientation of the magnetic particles that decreases the detected magnetization. NV centers provide optical detection of the interactions with molecular specificity.

It is clear that this thesis has just set a ground for many exciting directions where ABEL trap-like manipulation of single FNDs can be used in quantum sensing in the aqueous environments.

List of Acronyms

1D: one-dimensional

2D: two-dimensional

3D: three-dimensional

ABEL anti-Brownian electrokinetic trap

AFM: atomic force microscopy

DESM: deterministic emitter switch microscopy

FND: fluorescent nanodiamond

FP: fluorescent protein

FWHM: full width at half maximum

ISC intersystem crossing

NSOM: near-field scanning optical microscopy

NV: nitrogen vacancy

MRI: magnetic resonance imaging

MTB magnetotactic bacteria

ODMR: optically detected magnetic resonance

OT optical trap

QD quantum dot

PALM: photoactivated localization microscopy

PSB phonon side bands

RESOLFT: reversible saturable optical linear fluorescence transitions

SQUID: superconducting quantum interference device

SPT single particle tracking

STORM: stochastic optical reconstruction microscopy

ZFS: zero field splitting

References

1. Einstein, A., *On the movement of small particles suspended in stationary liquids required by the molecular-kinetic theory of heat.* Ann. d. Phys., 1905(17): p. 549-560.
2. Einstein, A., *Über die von der molekularkinetischen Theorie der Wärme geforderte Bewegung von in ruhenden Flüssigkeiten suspendierten Teilchen.* Annalen der Physik, 1905. **322**(8): p. 549-560.
3. Webb, J.l.P., *Einstein and Brownian motion-a student project.* Physics Education, 1980. **15**(2): p. 116.
4. Gaspard, P., et al., *Experimental evidence for microscopic chaos.* Nature, 1998. **394**(6696): p. 865-868.
5. Slomson, A.B., *Introduction to Combinatorics*. 1997: CRC Press.
6. Ashkin, A., *Forces of a single-beam gradient laser trap on a dielectric sphere in the ray optics regime.* Biophysical Journal, 1992. **61**(2): p. 569-582.
7. Ashkin, A., et al., *Observation of a single-beam gradient force optical trap for dielectric particles.* Optics Letters, 1986. **11**(5): p. 288-290.
8. Zemánek, P., A. Jonáš, and M. Liška, *Simplified description of optical forces acting on a nanoparticle in the Gaussian standing wave.* Journal of the Optical Society of America A, 2002. **19**(5): p. 1025-1034.
9. Seol, Y., A.E. Carpenter, and T.T. Perkins, *Gold nanoparticles: enhanced optical trapping and sensitivity coupled with significant heating.* Optics Letters, 2006. **31**(16): p. 2429-2431.
10. Krishnan, M., et al., *Geometry-induced electrostatic trapping of nanometric objects in a fluid.* Nature, 2010. **467**(7316): p. 692-695.
11. Tran, S.B.Q., P. Marmottant, and P. Thibault, *Fast acoustic tweezers for the two-dimensional manipulation of individual particles in microfluidic channels.* Applied Physics Letters, 2012. **101**(11): p. 114103.
12. Harris, N.R., et al., *A silicon microfluidic ultrasonic separator.* Sensors and Actuators B: Chemical, 2003. **95**(1–3): p. 425-434.
13. Tanyeri, M., et al., *A microfluidic-based hydrodynamic trap: design and implementation.* Lab on a Chip, 2011. **11**(10): p. 1786-1794.
14. Guan, W., et al., *Paul trapping of charged particles in aqueous solution.* Proceedings of the National Academy of Sciences, 2011. **108**(23): p. 9326-9330.
15. Smith, S., L. Finzi, and C. Bustamante, *Direct mechanical measurements of the elasticity of single DNA molecules by using magnetic beads.* Science, 1992. **258**(5085): p. 1122-1126.
16. Strick, T.R., et al., *The Elasticity of a Single Supercoiled DNA Molecule.* Science, 1996. **271**(5257): p. 1835-1837.
17. van der Heijden, T., et al., *Torque-limited RecA polymerization on dsDNA.* Nucleic Acids Research, 2005. **33**(7): p. 2099-2105.
18. Koster, D.A., et al., *Antitumour drugs impede DNA uncoiling by topoisomerase I.* Nature, 2007. **448**(7150): p. 213-217.
19. Itoh, H., et al., *Mechanically driven ATP synthesis by F1-ATPase.* Nature, 2004. **427**(6973): p. 465-468.
20. Gore, J., et al., *Mechanochemical analysis of DNA gyrase using rotor bead tracking.* Nature, 2006. **439**(7072): p. 100-104.
21. Barbic, M., et al., *Scanning probe electromagnetic tweezers.* Applied Physics Letters, 2001. **79**(12): p. 1897-1899.
22. Gosse, C. and V. Croquette, *Magnetic tweezers: micromanipulation and force measurement at the molecular level.* Biophysical Journal, 2002. **82**(6): p. 3314-3329.
23. Huckel, P.d.a.E., *The Cataphoresis of the Sphere.* Physikalische Zeitschrift, 1924(25): p. 204-210.
24. Fried, M. and D.M. Crothers, *Equilibria and Kinetics of Lac Repressor-Operator Interactions by Polyacrylamide-Gel Electrophoresis.* Nucleic Acids Research, 1981. **9**(23): p. 6505-6525.
25. Garner, M.M. and A. Revzin, *A Gel-Electrophoresis Method for Quantifying the Binding of Proteins to Specific DNA Regions - Application to Components of the Escherichia-Coli Lactose Operon Regulatory System.* Nucleic Acids Research, 1981. **9**(13): p. 3047-3060.
26. Chen, M.L., *Two-dimensional gel electrophoresis revealed antipsychotic drugs induced protein expression modulations in C6 glioma cells.* Prog Neuropsychopharmacol Biol Psychiatry, 2013. **40**: p. 1-11.
27. Xi, J., X.A. Si, and R. Gaide, *Electrophoretic Particle Guidance Significantly Enhances Olfactory Drug Delivery: A Feasibility Study.* PLoS ONE, 2014. **9**(1): p. e86593.
28. Swerdlow, H. and R. Gesteland, *Capillary gel electrophoresis for rapid, high resolution DNA sequencing.* Nucleic Acids Research, 1990. **18**(6): p. 1415-1419.
29. Karger, B.L. and A. Guttman, *DNA Sequencing by Capillary Electrophoresis.* Electrophoresis, 2009. **30**(Suppl 1): p. S196-S202.
30. von Smoluchowski, M., *Zur kinetischen Theorie der Brownschen Molekularbewegung und der Suspensionen.* Annalen der Physik, 1906. **326**(14): p. 756-780.
31. Nie, F.-Q., et al., *Robust monolithic silica-based on-chip electro-osmotic micro-pump.* Analyst, 2007. **132**(5): p. 417-424.
32. Meisel, I. and P. Ehrhard, *Electrically-excited (electroosmotic) flows in microchannels for mixing applications.* European Journal of Mechanics - B/Fluids, 2006. **25**(4): p. 491-504.
33. Henry, D.C., *The Cataphoresis of Suspended Particles. Part I. The Equation of Cataphoresis.* Proceedings of the Royal Society of London A: Mathematical, Physical and Engineering Sciences, 1931. **133**(821): p. 106-129.
34. Wang, Q. and W.E. Moerner, *Optimal strategy for trapping single fluorescent molecules in solution using the ABEL trap.* Applied Physics B-Lasers and Optics, 2010. **99**(1-2): p. 23-30.
35. Cohen, A.E. and W.E. Moerner, *Principal-components analysis of shape fluctuations of single DNA molecules.* Proceedings of the National Academy of Sciences, 2007. **104**(31): p. 12622-12627.
36. Goldsmith, R.H. and W.E. Moerner, *Watching conformational- and photodynamics of single fluorescent proteins in solution.* Nat Chem, 2010. **2**(3): p. 179-186.
37. Quimby, R.S., *Photonics and Lasers: An Introduction*. 2006, John Wiley & Sons. p. 323.

38. Sergio Martellucci, M.S., *Free and Guided Optical Beams*. 2004, World Scientific. p. 66.

39. Kalman, R.E., *A New Approach to Linear Filtering and Prediction Problems.* Transactions of the ASME – Journal of Basic Engineering, 1960(82 (Series D)): p. 35-45.

40. Galanis, G., et al., *Applications of Kalman filters based on non-linear functions to numerical weather predictions.* Annales Geophysicae, 2006. **24**: p. 2451-2460.

41. Foytik, J., P. Sankaran, and V. Asari, *Tracking and Recognizing Multiple Faces Using Kalman Filter and ModularPCA* Procedia Computer Science 2011. **6**: p. 256 - 261.

42. Walther, B., A. May, and T. Fischer, *Fitting Yield Curve Models Using the Kalman Filter.* PAMM, 2003. **3**(1): p. 507-508.

43. Fantian, K., et al. *Mobile Robot Localization Based on Extended Kalman Filter*. in *Intelligent Control and Automation, 2006. WCICA 2006. The Sixth World Congress on*. 2006.

44. Chalfie, M., et al., *Green fluorescent protein as a marker for gene-expression.* Science, 1994. **263**(5148): p. 802-805.

45. Griffin, B.A., S.R. Adams, and R.Y. Tsien, *Specific covalent labeling of recombinant protein molecules inside live cells.* Science, 1998. **281**(5374): p. 269-272.

46. Chan, W.C.W. and S.M. Nie, *Quantum dot bioconjugates for ultrasensitive nonisotopic detection.* Science, 1998. **281**(5385): p. 2016-2018.

47. Miyawaki, A., A. Sawano, and T. Kogure, *Lighting up cells: labelling proteins with fluorophores.* Nature Cell Biology, 2003: p. S1-S7.

48. Giepmans, B.N.G., et al., *Review - The fluorescent toolbox for assessing protein location and function.* Science, 2006. **312**(5771): p. 217-224.

49. Chang, Y.R., et al., *Mass production and dynamic imaging of fluorescent nanodiamonds.* Nature Nanotechnology, 2008. **3**(5): p. 284-288.

50. Yu, S.J., et al., *Bright fluorescent nanodiamonds: No photobleaching and low cytotoxicity.* Journal of the American Chemical Society, 2005. **127**(50): p. 17604-17605.

51. Wu, T.J., et al., *Tracking the engraftment and regenerative capabilities of transplanted lung stem cells using fluorescent nanodiamonds.* Nature Nanotechnology, 2013. **8**(9): p. 682-689.

52. Tisler, J., et al., *Highly Efficient FRET from a Single Nitrogen-Vacancy Center in Nanodiamonds to a Single Organic Molecule.* Acs Nano, 2011. **5**(10): p. 7893-7898.

53. Vaijayanthimala, V., et al., *The long-term stability and biocompatibility of fluorescent nanodiamond as an in vivo contrast agent.* Biomaterials, 2012. **33**(31): p. 7794-7802.

54. Han, K.Y., et al., *Three-Dimensional Stimulated Emission Depletion Microscopy of Nitrogen-Vacancy Centers in Diamond Using Continuous-Wave Light.* Nano Letters, 2009. **9**(9): p. 3323-3329.

55. Balasubramanian, G., et al., *Nanoscale imaging magnetometry with diamond spins under ambient conditions.* Nature, 2008. **455**(7213): p. 648-U46.

56. Dolde, F., et al., *Electric-field sensing using single diamond spins.* Nature Physics, 2011. **7**(6): p. 459-463.

57. Ziem, F.C., et al., *Highly Sensitive Detection of Physiological Spins in a Microfluidic Device.* Nano Letters, 2013. **13**(9): p. 4093-4098.

58. Kucsko, G., et al., *Nanometre-scale thermometry in a living cell.* Nature, 2013. **500**(7460): p. 54-U71.

59. Shi, F., et al., *Protein imaging. Single-protein spin resonance spectroscopy under ambient conditions.* Science, 2015. **347**(6226): p. 1135-8.

60. Aharonovich, I., et al., *Diamond-based single-photon emitters.* Reports on Progress in Physics, 2011. **74**(7).

61. Kayci, M., H.C. Chang, and A. Radenovic, *Electron Spin Resonance of Nitrogen-Vacancy Defects Embedded in Single Nanodiamonds in an ABEL Trap.* Nano Letters, 2014. **14**(9): p. 5335-5341.

62. Smith, B.R., et al., *Five-Nanometer Diamond with Luminescent Nitrogen-Vacancy Defect Centers.* Small, 2009. **5**(14): p. 1649-1653.

63. Fu, C.C., et al., *Characterization and application of single fluorescent nanodiamonds as cellular biomarkers.* Proceedings of the National Academy of Sciences of the United States of America, 2007. **104**(3): p. 727-732.

64. Guillois, O., G. Ledoux, and C. Reynaud, *Diamond infrared emission bands in circumstellar media.* Astrophysical Journal, 1999. **521**(2): p. L133-L136.

65. Goto, M., et al., *SPATIALLY RESOLVED 3 mu m SPECTROSCOPY OF ELIAS 1: ORIGIN OF DIAMONDS IN PROTOPLANETARY DISKS.* Astrophysical Journal, 2009. **693**(1): p. 610-616.

66. Vlasov, I.I., et al., *Molecular-sized fluorescent nanodiamonds.* Nature Nanotechnology, 2014. **9**(1): p. 54-58.

67. Chang, Y.R., et al., *Mass production and dynamic imaging of fluorescent nanodiamonds.* Nature Nanotechnology, 2008. **3**(5): p. 284-8.

68. Bradac, C., et al., *Observation and control of blinking nitrogen-vacancy centres in discrete nanodiamonds.* Nature Nanotechnology, 2010. **5**(5): p. 345-349.

69. Acosta, V.M., et al., *Temperature Dependence of the Nitrogen-Vacancy Magnetic Resonance in Diamond.* Physical Review Letters, 2010. **104**(7).

70. Doherty, M.W., et al., *Electronic Properties and Metrology Applications of the Diamond NV- Center under Pressure.* Physical Review Letters, 2014. **112**(4).

71. Steinert, S., et al., *Magnetic spin imaging under ambient conditions with sub-cellular resolution.* Nature Communications, 2013. **4**.

72. Childress, L., R. Walsworth, and M. Lukin, *Atom-like crystal defects: From quantum computers to biological sensors.* Physics Today, 2014. **67**(10): p. 38-43.

73. Chang, I.P., K.C. Hwang, and C.S. Chiang, *Preparation of Fluorescent Magnetic Nanodiamonds and Cellular Imaging.* Journal of the American Chemical Society, 2008. **130**(46): p. 15476-15481.

74. Hartl, A., et al., *Protein-modified nanocrystalline diamond thin films for biosensor applications.* Nature materials, 2004. **3**(10): p. 736-42.

75. Yang, W., et al., *DNA-modified nanocrystalline diamond thin-films as stable, biologically active substrates.* Nature materials, 2002. **1**(4): p. 253-7.

76. Bumb, A., et al., *Silica encapsulation of fluorescent nanodiamonds for colloidal stability and facile surface functionalization.* Journal of the American Chemical Society, 2013. **135**(21): p. 7815-8.

77. Resch-Genger, U., et al., *Quantum dots versus organic dyes as fluorescent labels.* Nature Methods, 2008. **5**(9): p. 763-775.

78. Tisler, J., et al., *Fluorescence and Spin Properties of Defects in Single Digit Nanodiamonds.* Acs Nano, 2009. **3**(7): p. 1959-1965.

79. Weber, G., *Fluorescence of riboflavin and flavin-adenine dinucleotide.* The Biochemical journal, 1950. **47**(1): p. 114-121.

80. Gohar, A.V., et al., *Subcellular localization-dependent changes in EGFP fluorescence lifetime measured by time-resolved flow cytometry.* Biomedical Optics Express, 2013. **4**(8): p. 1390-1400.

81. Sanchez-Andres, A., Y. Chen, and J.D. Muller, *Molecular brightness determined from a generalized form of Mandel's Q-parameter.* Biophysical Journal, 2005. **89**(5): p. 3531-3547.

82. Chen, Y., et al., *Molecular brightness characterization of EGFP in vivo by fluorescence fluctuation spectroscopy.* Biophysical Journal, 2002. **82**(1): p. 133-144.

83. Gaebel, T., et al., *Room-temperature coherent coupling of single spins in diamond.* Nature Physics, 2006. **2**(6): p. 408-413.

84. Santori, C., et al., *Indistinguishable photons from a single-photon device.* Nature, 2002. **419**(6907): p. 594-597.

85. He, Y.M., et al., *On-demand semiconductor single-photon source with near-unity indistinguishability.* Nature Nanotechnology, 2013. **8**(3): p. 213-217.

86. Wilson, A.C., et al., *Tunable spin-spin interactions and entanglement of ions in separate potential wells.* Nature, 2014. **512**(7512): p. 57-+.

87. Taylor, J.M., et al., *High-sensitivity diamond magnetometer with nanoscale resolution.* Nature Physics, 2008. **4**(10): p. 810-816.

88. Maze, J.R., et al., *Nanoscale magnetic sensing with an individual electronic spin in diamond.* Nature, 2008. **455**(7213): p. 644-U41.

89. Bending, S.J., *Local magnetic probes of superconductors.* Advances in Physics, 1999. **48**(4): p. 449-535.

90. Chang, A.M., et al., *Scanning Hall-Probe Microscopy of a Vortex and Field Fluctuations in La1.85sr0.15cuo4 Films.* Europhysics Letters, 1992. **20**(7): p. 645-650.

91. Budker, D., et al., *Resonant nonlinear magneto-optical effects in atoms.* Reviews of Modern Physics, 2002. **74**(4): p. 1153-1201.

92. Mamin, H.J., et al., *Nuclear magnetic resonance imaging with 90-nm resolution.* Nature Nanotechnology, 2007. **2**(5): p. 301-306.

93. Martin, Y., D.W. Abraham, and H.K. Wickramasinghe, *High-Resolution Capacitance Measurement and Potentiometry by Force Microscopy.* Applied Physics Letters, 1988. **52**(13): p. 1103-1105.

94. Neumann, P., et al., *High-Precision Nanoscale Temperature Sensing Using Single Defects in Diamond.* Nano Letters, 2013. **13**(6): p. 2738-2742.

95. Grinolds, M.S., et al., *Subnanometre resolution in three-dimensional magnetic resonance imaging of individual dark spins.* Nature Nanotechnology, 2014. **9**(4): p. 279-284.

96. Vanoort, E. and M. Glasbeek, *Electric-Field-Induced Modulation of Spin Echoes of N-V Centers in Diamond.* Chemical Physics Letters, 1990. **168**(6): p. 529-532.

97. Schirhagl, R., et al., *Nitrogen-Vacancy Centers in Diamond: Nanoscale Sensors for Physics and Biology.* Annual Review of Physical Chemistry, Vol 65, 2014. **65**: p. 83-105.

98. Mohan, N., et al., *In vivo imaging and toxicity assessments of fluorescent nanodiamonds in Caenorhabditis elegans.* Nano Letters, 2010. **10**(9): p. 3692-9.

99. Simpson, D.A., et al., *In vivo imaging and tracking of individual nanodiamonds in drosophila melanogaster embryos.* Biomedical Optics Express, 2014. **5**(4): p. 1250-1261.

100. Igarashi, R., et al., *Real-Time Background-Free Selective Imaging of Fluorescent Nanodiamonds in Vivo.* Nano Letters, 2012. **12**(11): p. 5726-5732.

101. Chang, C.C., et al., *Exploring cytoplasmic dynamics in zebrafish yolk cells by single particle tracking of fluorescent nanodiamonds.* Advances in Photonics of Quantum Computing, Memory, and Communication V, 2012. **8272**.

102. Huang, Y.A., et al., *The effect of fluorescent nanodiamonds on neuronal survival and morphogenesis.* Scientific Reports, 2014. **4**.

103. Hui, Y.Y., et al., *Wide-field imaging and flow cytometric analysis of cancer cells in blood by fluorescent nanodiamond labeling and time gating.* Scientific Reports, 2014. **4**.

104. McGuinness, L.P., et al., *Quantum measurement and orientation tracking of fluorescent nanodiamonds inside living cells.* Nature Nanotechnology, 2011. **6**(6): p. 358-363.

105. Manus, L.M., et al., *Gd(III)-nanodiamond conjugates for MRI contrast enhancement.* Nano Letters, 2010. **10**(2): p. 484-9.

106. Deschout, H., et al., *Precisely and accurately localizing single emitters in fluorescence microscopy.* Nature Methods, 2014. **11**(3): p. 253-266.

107. Rittweger, E., et al., *STED microscopy reveals crystal colour centres with nanometric resolution.* Nature Photonics, 2009. **3**(3): p. 144-147.

108. Kuhn, S., et al., *Diamond colour centres as a nanoscopic light source for scanning near-field optical microscopy.* Journal of Microscopy-Oxford, 2001. **202**: p. 2-6.

109. Nakayama, Y., et al., *Tunable nanowire nonlinear optical probe.* Nature, 2007. **447**(7148): p. 1098-U8.

110. Dutto, F., et al., *Nonlinear Optical Response in Single Alkaline Niobate Nanowires.* Nano Letters, 2011. **11**(6): p. 2517-2521.

111. Dutto, F. and A. Radenovic, *Alkaline niobate nanowires as opto-mechanical probes.* Optical Trapping and Optical Micromanipulation Ix, 2012. **8458**.

112. Macias-Romero, C., et al., *Probing Rotational and Translational Diffusion of Nanodoublers in Living Cells on Microsecond Time Scales.* Nano Letters, 2014. **14**(5): p. 2552-2557.

113. Mor, F.M., et al., *Upconversion Particle as a Local Luminescent Brownian Probe: A Photonic Force Microscopy Study.* Acs Photonics, 2014. **1**(12): p. 1251-1257.

114. Betzig, E., et al., *Near-Field Scanning Optical Microscopy (Nsom) - Development and Biophysical Applications.* Biophysical Journal, 1986. **49**(1): p. 269-279.

115. Durig, U., D.W. Pohl, and F. Rohner, *Near-Field Optical-Scanning Microscopy.* Journal of Applied Physics, 1986. **59**(10): p. 3318-3327.

116. Betzig, E., et al., *Breaking the Diffraction Barrier - Optical Microscopy on a Nanometric Scale.* Science, 1991. **251**(5000): p. 1468-1470.

117. Sonnefraud, Y., et al., *Diamond nanocrystals hosting single nitrogen-vacancy color centers sorted by photon-correlation near-field microscopy.* Optics Letters, 2008. **33**(6): p. 611-613.

118. Einstein, A., *Strahlungs-Emission und -Absorption nach der Quantentheorie.* Deutsche Physikalische Gesellschaft, 1916. **18**: p. 318-323.

119. Hell, S.W. and J. Wichmann, *Breaking the Diffraction Resolution Limit by Stimulated-Emission - Stimulated-Emission-Depletion Fluorescence Microscopy.* Optics Letters, 1994. **19**(11): p. 780-782.

120. Klar, T.A. and S.W. Hell, *Subdiffraction resolution in far-field fluorescence microscopy.* Optics Letters, 1999. **24**(14): p. 954-6.

121. Hell, S.W., *Far-field optical nanoscopy.* Science, 2007. **316**(5828): p. 1153-1158.

122. Arroyo-Camejo, S., et al., *Stimulated emission depletion microscopy resolves individual nitrogen vacancy centers in diamond nanocrystals.* Acs Nano, 2013. **7**(12): p. 10912-9.

123. Maurer, P.C., et al., *Far-field optical imaging and manipulation of individual spins with nanoscale resolution.* Nature Physics, 2010. **6**(11): p. 912-918.

124. Betzig, E., et al., *Imaging intracellular fluorescent proteins at nanometer resolution.* Science, 2006. **313**(5793): p. 1642-1645.

125. Hess, S.T., T.P.K. Girirajan, and M.D. Mason, *Ultra-high resolution imaging by fluorescence photoactivation localization microscopy.* Biophysical Journal, 2006. **91**(11): p. 4258-4272.

126. Rust, M.J., M. Bates, and X.W. Zhuang, *Sub-diffraction-limit imaging by stochastic optical reconstruction microscopy (STORM).* Nature Methods, 2006. **3**(10): p. 793-795.

127. Chen, E.H., et al., *Wide-Field Multispectral Super-Resolution Imaging Using Spin-Dependent Fluorescence in Nanodiamonds.* Nano Letters, 2013. **13**(5): p. 2073-2077.

128. Le Sage, D., et al., *Optical magnetic imaging of living cells.* Nature, 2013. **496**(7446): p. 486-U105.

129. Eder, S.H.K., et al., *Magnetic characterization of isolated candidate vertebrate magnetoreceptor cells.* Proceedings of the National Academy of Sciences of the United States of America, 2012. **109**(30): p. 12022-12027.

130. Cuche, A., et al., *Near-field optical microscopy with a nanodiamond-based single-photon tip.* Optics Express, 2009. **17**(22): p. 19969-19980.

131. Fedotov, I.V., et al., *Electron spin manipulation and readout through an optical fiber.* Scientific Reports, 2014. **4**.

132. Maletinsky, P., et al., *A robust scanning diamond sensor for nanoscale imaging with single nitrogen-vacancy centres.* Nature Nanotechnology, 2012. **7**(5): p. 320-324.

133. Degen, C.L., *Scanning magnetic field microscope with a diamond single-spin sensor.* Applied Physics Letters, 2008. **92**(24).

134. Ofori-Okai, B.K., et al., *Spin properties of very shallow nitrogen vacancy defects in diamond.* Physical Review B, 2012. **86**(8).

135. Horowitz, V.R., et al., *Electron spin resonance of nitrogen-vacancy centers in optically trapped nanodiamonds.* Proceedings of the National Academy of Sciences of the United States of America, 2012. **109**(34): p. 13493-13497.

136. Geiselmann, M., et al., *Three-dimensional optical manipulation of a single electron spin.* Nature Nanotechnology, 2013. **8**(3): p. 175-179.

137. Svoboda, K. and S.M. Block, *Optical Trapping of Metallic Rayleigh Particles.* Optics Letters, 1994. **19**(13): p. 930-932.

138. Fields, A.P. and A.E. Cohen, *Electrokinetic trapping at the one nanometer limit.* Proceedings of the National Academy of Sciences of the United States of America, 2011. **108**(22): p. 8937-8942.

139. Maclaurin, D., et al., *Nanoscale magnetometry through quantum control of nitrogen-vacancy centres in rotationally diffusing nanodiamonds.* New Journal of Physics, 2013. **15**.

140. Geiselmann, M., et al., *Three-dimensional optical manipulation of a single electron spin.* Nat Nanotechnol, 2013. **8**(3): p. 175-9.

141. Peterman, E.J., F. Gittes, and C.F. Schmidt, *Laser-induced heating in optical traps.* Biophys J, 2003. **84**(2 Pt 1): p. 1308-16.

142. Gosse, C. and V. Croquette, *Magnetic tweezers: micromanipulation and force measurement at the molecular level.* Biophys J, 2002. **82**(6): p. 3314-29.

143. Wu, M.C., *Optoelectronic tweezers.* Nature Photonics, 2011. **5**(6): p. 322-324.

144. Tran, S.B.Q., P. Marmottant, and P. Thibault, *Fast acoustic tweezers for the two-dimensional manipulation of individual particles in microfluidic channels.* Applied Physics Letters, 2012. **101**(11).

145. Guan, W.H., et al., *Paul trapping of charged particles in aqueous solution.* Proceedings of the National Academy of Sciences of the United States of America, 2011. **108**(23): p. 9326-9330.

146. Zhuang, Z.Y., et al., *The effect of surface tethering on the folding of the src-SH3 protein domain.* Physical Biology, 2009. **6**(1).

147. King, J.K., *Three-Dimensional Electrokinetic Trapping of a Single Fluorescent Nanoparticle in Solution*, 2013.

148. Bockenhauer, S.D. and W.E. Moerner, *Photo-induced conformational flexibility in single solution-phase peridinin-chlorophyll-proteins.* The journal of physical chemistry. A, 2013. **117**(35): p. 8399-406.

149. Cohen, A.E. and W.E. Moerner. *An all-glass microfluidic cell for the ABEL trap: fabrication and modeling*. 2005.

150. King, J.K., B.K. Canfield, and L.M. Davis, *Three-dimensional anti-Brownian electrokinetic trapping of a single nanoparticle in solution.* Applied Physics Letters, 2013. **103**(4): p. 043102.

151. Speidel, M., A. Jonas, and E.L. Florin, *Three-dimensional tracking of fluorescent nanoparticles with subnanometer precision by use of off-focus imaging.* Optics Letters, 2003. **28**(2): p. 69-71.

152. Kayci, M., H.-C. Chang, and A. Radenovic, *Electron spin resonance of nitrogen-vacancy defects embedded in single nanodiamonds in an ABEL trap.* Nano letters, 2014. **14**(9): p. 5335-5341.

153. Davies, G. and M.F. Hamer, *Optical Studies of 1.945 Ev Vibronic Band in Diamond.* Proceedings of the Royal Society of London Series a-Mathematical and Physical Sciences, 1976. **348**(1653): p. 285-298.

154. Gruber, A., et al., *Scanning confocal optical microscopy and magnetic resonance on single defect centers.* Science, 1997. **276**(5321): p. 2012-2014.

155. Babinec, T.M., et al., *A diamond nanowire single-photon source.* Nature Nanotechnology, 2010. **5**(3): p. 195-199.

156. Englund, D., et al., *Deterministic Coupling of a Single Nitrogen Vacancy Center to a Photonic Crystal Cavity.* Nano Letters, 2010. **10**(10): p. 3922-3926.

157. Pauzauskie, P.J., et al., *Optical trapping and integration of semiconductor nanowire assemblies in water.* Nature Materials, 2006. **5**(2): p. 97-101.

158. Ashkin, A., *Optical trapping and manipulation of neutral particles using lasers.* Proc. Natl. Acad. Sci. USA, 1997. **94**: p. 4853-4860.

159. Cohen, A.E. and W.E. Moerner, *Method for trapping and manipulating nanoscale objects in solution.* Applied Physics Letters, 2005. **86**(9).

160. Wang, Q., et al., *Probing Single Biomolecules in Solution Using the Anti-Brownian Electrokinetic (ABEL) Trap.* Accounts of Chemical Research, 2012. **45**(11): p. 1955-1964.

161. A.P. Fields, A.E.C., *Anti-Brownian Traps for Studies on Single Molecules*, in *Methods in Enzymology*, E. Inc., Editor. 2010.

162. Cohen, A.E. and W.E. Moerner, *Principal-components analysis of shape fluctuations of single DNA molecules.* Proceedings of the National Academy of Sciences of the United States of America, 2007. **104**(31): p. 12622-12627.

163. Wang, Q. and W.E. Moerner, *An Adaptive Anti-Brownian Electrokinetic Trap with Real-Time Information on Single-Molecule Diffusivity and Mobility.* Acs Nano, 2011. **5**(7): p. 5792-5799.

164. Goldsmith, R.H. and W.E. Moerner, *Watching conformational- and photodynamics of single fluorescent proteins in solution.* Nature Chemistry, 2010. **2**(3): p. 179-186.

165. Bockenhauer, S., et al., *Conformational Dynamics of Single G Protein-Coupled Receptors in Solution.* Journal of Physical Chemistry B, 2011. **115**(45): p. 13328-13338.

166. Wang, Q. and W.E. Moerner, *Lifetime and Spectrally Resolved Characterization of the Photodynamics of Single Fluorophores in Solution Using the Anti-Brownian Electrokinetic Trap.* Journal of Physical Chemistry B, 2013. **117**(16): p. 4641-4648.

167. Rendler, T., et al., *Monitoring single membrane protein dynamics in a liposome manipulated in solution by the ABELtrap.* Imaging, Manipulation, and Analysis of Biomolecules, Cells, and Tissues Ix, 2011. **7902**.

168. Mochalin, V.N., et al., *The properties and applications of nanodiamonds.* Nature Nanotechnology, 2012. **7**(1): p. 11-23.

169. Felton, S., et al., *Hyperfine interaction in the ground state of the negatively charged nitrogen vacancy center in diamond.* Physical Review B, 2009. **79**(7).

170. Smeltzer, B., J. McIntyre, and L. Childress, *Robust control of individual nuclear spins in diamond.* Physical Review A, 2009. **80**(5).

171. Steiner, M., et al., *Universal enhancement of the optical readout fidelity of single electron spins at nitrogen-vacancy centers in diamond.* Physical Review B, 2010. **81**(3).

172. Acosta, V.M., et al., *Broadband magnetometry by infrared-absorption detection of nitrogen-vacancy ensembles in diamond.* Applied Physics Letters, 2010. **97**(17).

173. Simon, D., *Optimal state estimation: Kalman, H infinity, and nonlinear approaches*. 2006: John Wiley & Sons.

174. Epstein, R.J., et al., *Anisotropic interactions of a single spin and dark-spin spectroscopy in diamond.* Nature Physics, 2005. **1**(2): p. 94-98.

175. Dumeige, Y., et al., *Controling the single-diamond nitrogen-vacancy color center photoluminescence spectrum with a Fabry-Perot microcavity.* New Journal of Physics, 2011. **13**.

176. Cang, H., C. Shan Xu, and H. Yang, *Progress in single-molecule tracking spectroscopy.* Chemical Physics Letters, 2008. **457**(4–6): p. 285-291.

177. Wells, N.P., et al., *Time-Resolved Three-Dimensional Molecular Tracking in Live Cells.* Nano Letters, 2010. **10**(11): p. 4732-4737.

178. Yao, L. and S. Xu, *Force-Induced Remnant Magnetization Spectroscopy for Specific Magnetic Imaging of Molecules.* Angewandte Chemie International Edition, 2011. **50**(19): p. 4407-4409.

179. De Silva, L., et al., *Well-Defined and Sequence-Specific Noncovalent Binding Forces of DNA.* The Journal of Physical Chemistry B, 2013. **117**(25): p. 7554-7558.

180. De Silva, L., L. Yao, and S. Xu, *Mechanically resolving noncovalent bonds using acoustic radiation force.* Chemical Communications, 2014. **50**(74): p. 10786-10789.

Metin Kayci

metin.kayci@epfl.ch, +41786920488

Education & Experiences

9/2011-present	Ph.D. in Photonics
	Ecole Polytechnique Fédérale de Lausanne -EPFL- (Switzerland)
	Thesis: Nanoscale magnetometry with single FNDs manipulated in Anti-Brownian electrokinetic trap.
5/2010-9/2010	Summer Research at MIT, EECS department (USA).
	Implementation of a compact optoelectronic neural coprocessor (CONCOP).
9/2007-6/2011	B.Sc. in Electronics Engineering (ranked 1st), minor in Physics (ranked 1st)
	Sabanci University (Turkey)

Skills

Technical	Photolithography, e-beam lithography, thin film deposition, dry and wet etching, soft lithography, microfluidics design/fabrication, free-space optics, fluorescence microscopy, nonlinear optics, RF circuit design/fabrication, MEMS.
Computation	FPGA, C++, LabVIEW, Matlab, COMSOL Multiphysics, SOLIDWORKS, ImageJ, CAD

Academic works

Spring 2011-2013	Fundamental of bio-photonics (TA)
Fall 2010-2011	Optoelectronics (TA)
Spring 2009-2010	Electronic circuits II (TA)

Publications

Journal Articles

1. **M. Kayci**, A. Radenovic. Single fluorescent nanodiamond in a three-dimensional ABEL trap. *Scientific Reports* (1015)
2. **M. Kayci**, H.C. Chang, A. Radenovic. Electron Spin Resonance of Nitrogen-Vacancy Defects Embedded in Single Nanodiamonds in an ABEL Trap. *Nano Lett*ers (2014)
3. O. L. Sanchez, D. Lembke, **M. Kayci**, A. Radenovic & A. Kis. Ultrasensitive photodetectors based on monolayer MoS_2. *Nature Nanotechnology* (2013)

Oral Presentations

1. Single nano diamonds as scanning magnetometer in a fluidic environment, *ENEFM & INTERM 2015*, Mugla (Turkey), October 19th-23rd 2015.
2. Optically detected magnetic resonance spectrum of single FNDs in aqueous medium, *ICDCM 2014*, Madrid (spain), September 7th-11th 2014.
3. Electron spin resonance of nitrogen-vacancy centers in single nano diamond particles, *NDNC 2014*, Chicago (USA), May 25th-29th 2014.

Posters

1. RF antenna integrated ABEL trap for electron spin resonance measurements, *EPFL Photonics Day*, Lausanne, November 14th 2014.
2. Electrokinetic trap of nano-scale particles in microfluidics, *Joint Annual Meeting of the Austrian Physical Society and the Swiss Physical Society*, Linz (Austria), September 3rd-6th 2013.
3. Nanopore integrated Anti-Brownian Electrokinetic trap, *Swiss Single Molecule Localization Microscopy Symposium,* Lausanne (Switzerland), August 29th-31st 2012.

Languages: Kurdish (native), Turkish, English